

Piezoelectric energy harvesting using mechanical metamaterials and phononic crystals

Geon Lee^{1,5}, Dongwoo Lee ^{1,5}, Jeonghoon Park¹, Yeongtae Jang¹, Miso Kim² & Junsuk Rho ^{1,3,4}✉

Mechanical metamaterials and phononic crystals enable localizing, focusing, and guiding of elastic or acoustic waves in various ways. Here, we describe the physical mechanisms underpinning wave manipulation and then review the most recent energy harvesting methods for converting localized mechanical wave energy to useable electrical energy. Due to the exceptional wave-matter interactions enabled by the man-made structures, energy is collected more efficiently than through conventional methods. Artificially designed mechanical structures are versatile, especially when used in renewable and ecologically-benign energy transformation, and have a wide array of potential applications.

Waves such as vibration (elastic waves), sound (acoustic waves), and light (electromagnetic waves) are ubiquitous in nature, and each interacts with matter in their own different way, each with its own energy. However, most of the energy is dissipated through mechanisms such as material damping, friction, and heat transfer. To repurpose such waste energy, researchers have been looking for sustainable and ecologically-benign energy sources that harvest waste energy and convert it to electrical energy with high efficiency. The method of energy capture relies on the wave type to be converted and how it is to be converted, therefore the use of transducers varies accordingly. For example, piezoelectric materials are used for elastic and acoustic waves^{1,2}, pyroelectric materials for thermal waves^{3,4}, and solar cells for sunlight^{5,6}. Piezoelectric materials yield voltage by electrical polarization when subjected to an applied force⁷. This phenomenon happens when external mechanical stimuli cause changes that align the direction of molecular dipole moments. To greatly increase the effect of electrical polarization which increases proportionally to the displacement of the medium, the medium should be subjected to high stress. However, existing piezoelectric energy harvesting (PEH) materials have practical limits in terms of efficiency and frequency range, making them unsuitable for use with electrical devices.

Metamaterials (MMs) are man-made structures with properties that are not found in naturally-occurring materials. Veselago pioneered the field of MMs by proposing theoretical research into materials in which the refractive index becomes negative as a result of the unnatural electromagnetic responses⁸. Pendry later proposed MMs that operate in narrow frequency ranges by using split-ring resonators with negative permeability^{9,10}. Smith has experimentally developed a negative refractive index in the microwave regime, leveraging theoretical grounds¹¹. Since then, electromagnetic MM research has been lively, leading to the control of acoustic^{12–16}, elastic^{17–20}, and seismic^{21,22} waves being investigated in recent years. Progress in MMs has been possible due to mathematical analogies in the underlying wave physics. PEH-generated mechanical (elastic and acoustic) waves can be described using constitutive parameters such as mass density and modulus, both of which are usually positive. However, MMs allow for

¹Department of Mechanical Engineering, Pohang University of Science and Technology (POSTECH), Pohang, Republic of Korea. ²School of Advanced Materials Science and Engineering, Sungkyunkwan University, Suwon, Republic of Korea. ³Department of Chemical Engineering, Pohang University of Science and Technology (POSTECH), Pohang, Republic of Korea. ⁴POSCO-POSTECH-RIST Convergence Research Center for Flat Optics and Metaphotonics, Pohang, Republic of Korea. ⁵These authors contributed equally: Geon Lee, Dongwoo Lee. ✉email: jsrho@postech.ac.kr

negative mass density and negative elastic modulus from discrete mass-spring equivalent models in dynamic systems. Milton and Willis explained the physical concept of effective mass density theoretically²³, which Yao later validated experimentally²⁴. In mass-in-mass systems, the local resonance mechanism can result in a negative effective mass density. Moreover, as demonstrated experimentally by Fang²⁵, a negative effective bulk modulus can be obtained using membrane systems or Helmholtz resonators. Negative parameters have significant consequences because they imply that the amplitude of a wave can decay exponentially by reshaping the forward propagation wave into an evanescent wave. The decaying wave remains as a localized wave in a small segment of the structure and its energy can be efficiently converted by attaching a piezoelectric material to the local area. These MMs are specially designed by tailoring the shapes, sizes, and periodic configurations of subwavelength resonant elements, known as meta-atoms. As a result, unique properties such as negative constitutive parameters and remarkable phenomena in frequency spectra across Bloch states have been discovered, and extended to nonlocality^{26–28}, non-Hermitian^{29–31} systems, and topological^{32–34} effects for intriguing behaviors. Media of periodic structures ranging from isotropy to bianisotropy^{35,36} in the constitutive parameter set have potential applications in a variety of domains of wave physics.

The notion of phononic crystals (PnCs) is similar to that of photonic crystals^{37,38}, in that both evolved from electronic systems that forbid certain energy-level bands. PnCs are periodic structures that exploit Bragg scattering in lattices to take advantage of wave interference induced by a high-impedance mechanical contrast between hosts and inclusions. The interference arises when the wavelength is of the same order as the lattice constant of the periodic structure, and thereby allows interference with scattered waves in neighboring lattices. PnCs are characterized by a bandgap or frequency range in which waves cannot propagate through a medium. Using PEH, the bandgap mechanism can be used efficiently to localize and focus waves. Surprisingly, an extremely high wave localization can be induced in imperfect structures by exploiting defect cavity modes. Furthermore, by adjusting the refractive index of each crystal size, PnC arrays that consist of a gradient of crystal sizes contribute to increased wave focusing and yield a gradient-index (GRIN) lens. The refractive index is inversely proportional to the phase velocity, so the incoming plane wave bends when the phase velocities form a gradient. By carefully manipulating the refractive indices, the waves can be captured at the focal point. Because of a lack of rigorous classification, the terms MM and PnC, which give rise to unusual features, are commonly used interchangeably. The lattice spacing, which corresponds to the range of working frequency, provides an intuitive way of understanding the distinction: MMs are composed of a cluster of strong dispersive resonators that operate on the subwavelength scale, whereas PnCs are composed of multiple scatterers that operate on the wavelength scale.

Vibration insulators^{39–42}, soundproofing^{43,44}, and seismic mitigation^{45,46} structures are just a few of the cutting-edge applications inspired by MM and PnC platforms. Parallel to theoretical progress, fabrication techniques such as 3D printing^{47–49} and structuring of macro- and nano-scale designs for MMs and PnCs have been developed. Wireless networks, portable and wearable devices, sensors, the Internet of Things following the Fourth Industrial Revolution, and biotechnology devices have all seen substantial growth. Related products frequently use batteries that have a lifetime and may require special disposal, therefore, PEH research is being conducted to develop a new generation of energy sources to address such challenges. MMs and PnCs improve energy harvesting efficiency by redirecting the wave energy input to the desired position for maximal

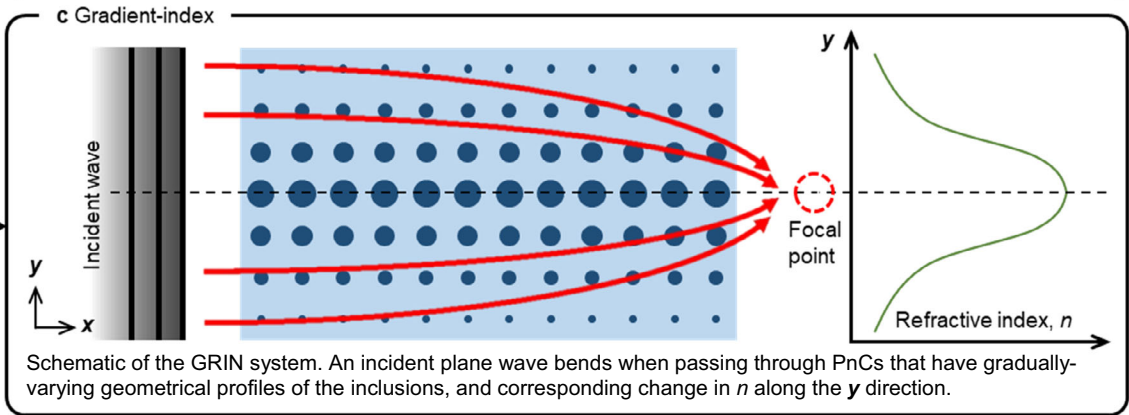
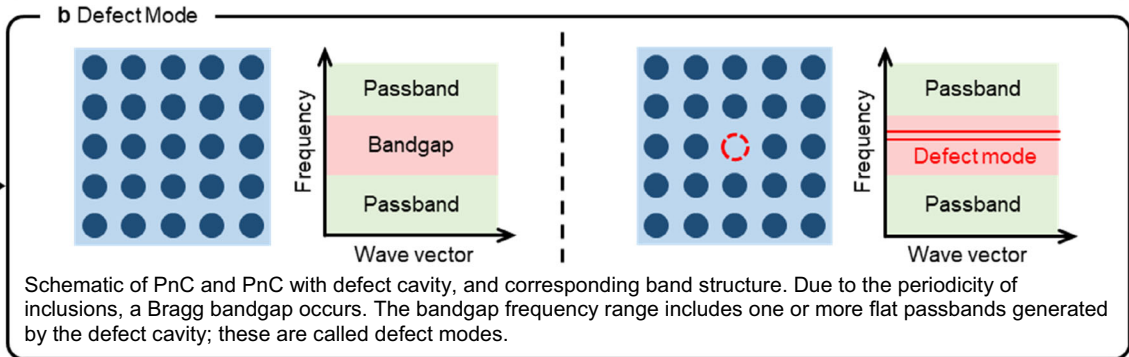
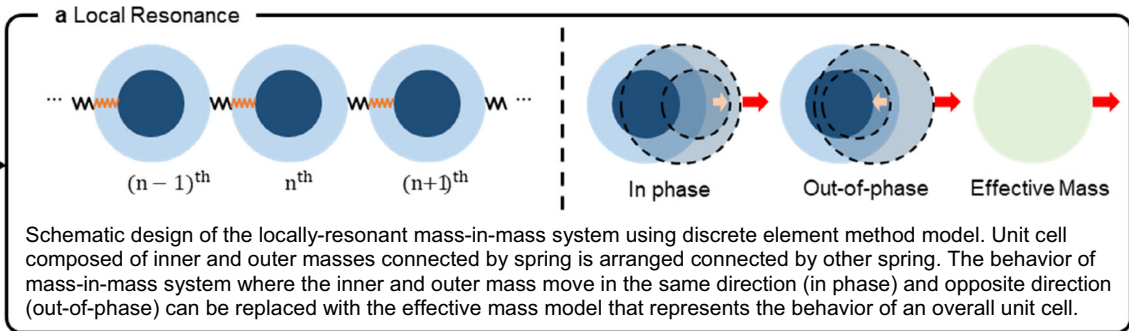
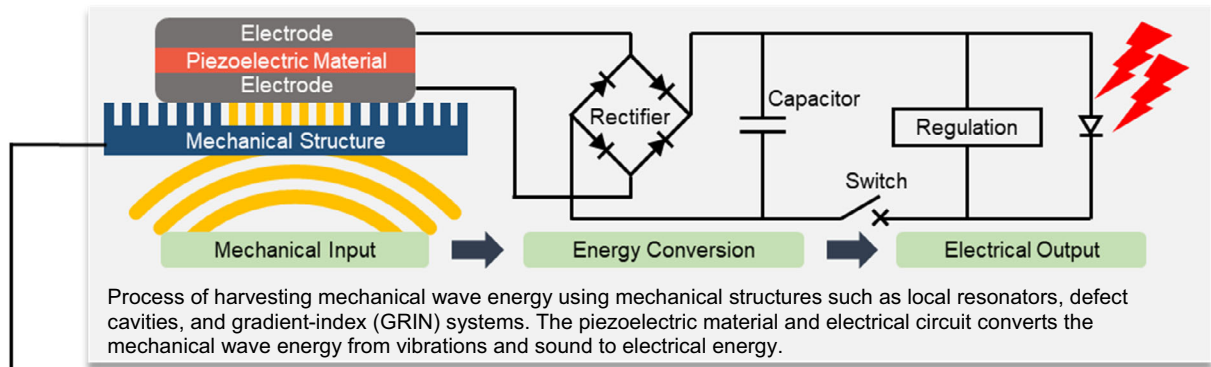
energy conversion and harvesting. In this Review, we describe methods for capturing the energy of mechanical waves at broadband frequencies and achieving effective PEH by using MMs and PnCs, which are wavelength- or subwavelength-scale microstructures integrated with piezoelectric materials. Moreover, we place a greater emphasis on the physical meaning and discuss it in wider context than earlier publications^{50,51} as a useful indicator for future research directions in this area. We provide an overview of wave localization and focusing methods and applications that make use of local resonances, defect modes, and GRIN structures that convert mechanical energy to electrical energy through integrated piezoelectric devices (Box 1).

Physical mechanism of local resonance in MMs. To be used for PEH, the MMs should include meta-atoms with an independent degree of freedom capable of triggering local resonances. The first elastic meta-atom with local resonance consisted of relatively high-density solid-core materials and epoxy-enclosed soft coatings⁵². When the operational frequency of the driving force coincided with the natural frequency of the inner core mass, which is a resonating element, a state known as a local resonance is obtained. Following that, the effective mass of the mass-in-mass equivalent model⁵³ was developed to describe the out-of-phase and in-phase motions of the outer mass and internal mass (Box 1a). The sign indicates the direction of movement, and the effective mass moves in the same direction as the main mass.

Under dynamic settings, mechanical waves can propagate through mechanical MMs in a specific frequency range known as the passband but not in the stopband (or bandgap)⁵⁴. Two fundamental mechanisms can drive the bandgap: Bragg scattering and local resonances^{55–57}. When the wavelength in a periodic array is equivalent to the lattice constant, PnCs undergo Bragg scattering, which results in bandgaps due to interference. MMs, on the other hand, exhibit local resonances, which can also produce bandgaps when the wavelength is much larger than the lattice constant. According to the mass-in-mass equivalent model, in a local resonance state, the effective mass can become negative near the resonant frequency, and the dynamic structural response results in an out-of-phase oscillation compared to the in-phase input force. Due to the out-of-phase oscillations, the resultant force approaches zero at the resonant frequency, i.e., the displacement movement is considerably suppressed, and the accumulated energy remains inside the resonators. Meanwhile, without real-valued wavenumbers in the bandgap of either Bragg scattering or local resonances, waves cannot propagate in the medium, and instead convergent and divergent imaginary-valued components appear. For local resonances, the imaginary values globally support a lossy system that loses the frequency components that are locally trapped in resonators. The PEH is generated by mounting a piezoelectric device at the place where wave energy is localized and converting it to electrical energy. The harvesting efficiency of the PEH using MMs is higher than that of a conventional piezoelectric substrate.

PEH systems using locally resonant MMs. Numerous designs, including beams and plates, have been utilized in locally resonant MMs. Due to the high Q-factor associated with the resonance mechanism and the relatively narrow range of the resonating frequency, such MMs with an augmented mass are well geared for efficient PEH. For this reason, the local-resonance mechanism can have dual functionalities, simultaneously contributing towards both wave attenuation and energy harvesting. Gonella et al.⁵⁸ developed a cantilever PEH with piezoelectric microstructures that makes use of the bandgap mechanism. The wave filtering effect is dramatically enhanced due to the bandgap, and

Box 1 | Mechanical piezoelectric energy harvesting (PEH) using metamaterials (MMs) and phononic crystals (PnCs)



energy harvesting is achieved as a consequence of the conversion of the localized kinetic energy. Mikoshiba et al.⁵⁹ used an array of dual functional resonators based on local resonance with electromagnetic induction to establish energy harvesting of elastic waves both analytically and experimentally. Ahmed and

Banerjee⁶⁰ designed an acoustic-MM energy harvester embedded in a soft matrix with a piezoelectric wafer that yields the capability of large electrical potential and power. The following sections discuss the latest studies indicating that employing MMs with local resonances may further improve the efficiency of PEH.

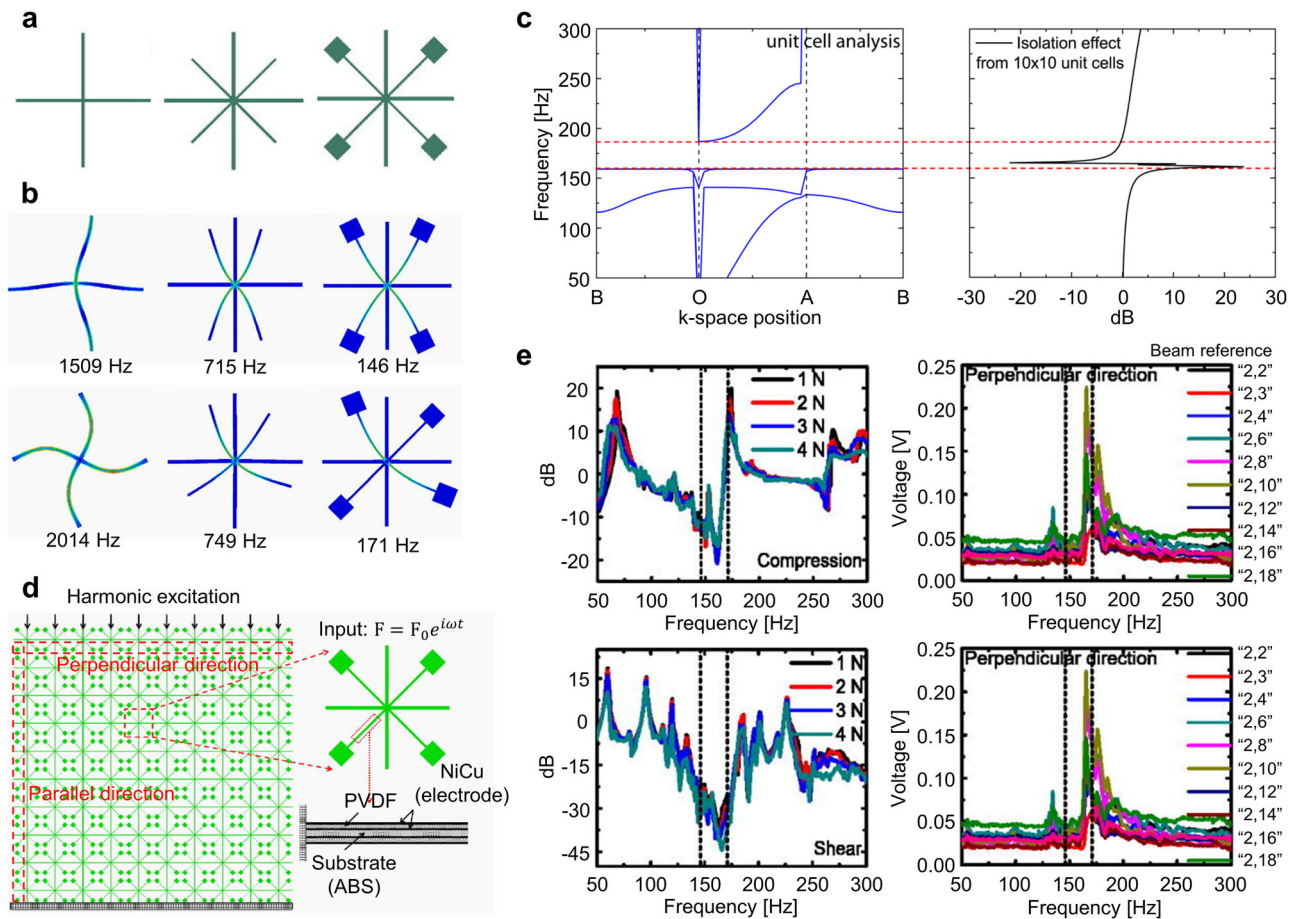


Fig. 1 Mechanical metamaterial (MM) consisting of locally resonant cantilevers for energy harvesting. **a** Topologies of the unit cell: Original square lattice, modified square lattice with cantilevers attached, and modified square lattice with cantilevers and masses attached. **b** Representative mode shapes of each unit cell. **c** Comparison of the force transmission spectrum to a band structure obtained from unit cell analysis by sweeping the wavevector along the contour of the irreducible Brillouin zone. **d** Array of mechanical MMs for energy harvesting. Piezoelectric material (polyvinylidene fluoride film (PVDF)) is attached at the substrate (acrylonitrile butadiene styrene (ABS) plastic) to convert localized kinetic energy to electrical energy. **e** Capability of designed MMs to filter mechanical waves: Compression longitudinal-wave test and shear transverse-wave test. “X, Y”: number of cantilevers in perpendicular and parallel directions to excitation, respectively. Within the bandgap range indicated by dashed lines, the waves do not propagate. The energy harvesting capability with longitudinal wave input force 5.34 N: Cantilevers in perpendicular and parallel directions to the excitations. Maximum output of voltage and power is found within the bandgap frequency measured across a 1-MW resistor⁶¹. Reprinted with permission from ref. ⁶¹.

Li et al.⁶¹ designed a cantilever MM for dual-purpose PEH (Fig. 1a). The MM is partitioned into a free-standing cantilever and a primary structural frame, with vibrations at natural bending frequencies localized in the middle of the cantilever rather than at the nodal point (intersection) between them (Fig. 1b). Cantilevers behave as local resonators, and their PEH efficiency can be improved by increasing their stiffness and inertia. A clear bandgap frequency range can be obtained by calculating the band structure and the force transmission spectra (Fig. 1c). Elastic waves are obviously forbidden in the bandgap but are locally confined throughout the system, particularly at the cantilevers. Each harmonic vibration of the free-standing cantilever and the primary structural frame is engaged in the strongly-coupled mode when the harmonic elastic bulk wave is well synchronized with the vibration of the cantilever. In this scenario, the vibration energy delivered by the elastic bulk wave is accumulated by the resonance of the cantilever, where it is converted to localized kinetic energy. A piezoelectric polymer thin film (polyvinylidene fluoride (PVDF) film) with electrodes was attached to each cantilever for further conversion of kinetic energy to electrical energy, providing dual functionalities of vibration isolation and energy harvesting into a single device

(Fig. 1d). Indeed, the primary structure that is interconnected to each beam does not undergo significant elastic deformation, but the well-confined vibration energy is trapped locally in the substructure. Consequently, elastic waves become suppressed externally, and the remaining strong strain fields are generated by energy localization; this reaction implies that cantilever deformation would result in efficient energy conversion. This design was intended to filter out noise from mechanical vibration. To do this, an extra mass was attached to the end of the cantilever to lower its cutoff frequency. Kinetic-to-electric energy conversion is also accessible using the piezoelectric response of the PVDF film transducer; this conversion shares the same mechanism as the case in which no extra mass is required. When stimulated at the resonant frequency, the use of an energy harvester at the corresponding frequencies produce a voltage output (Fig. 1e). Due to the anisotropic design, both compression (perpendicular) and shear (parallel) loadings were considered. Given that the complete bandgap is obtained along high-symmetry lines, the vibration-isolation effect emerges regardless of the direction of the excited waves. When an input force of 5.34 N was applied perpendicular to the direction of the force, the PVDF film produced a maximum output voltage of 0.22 V, a maximum load

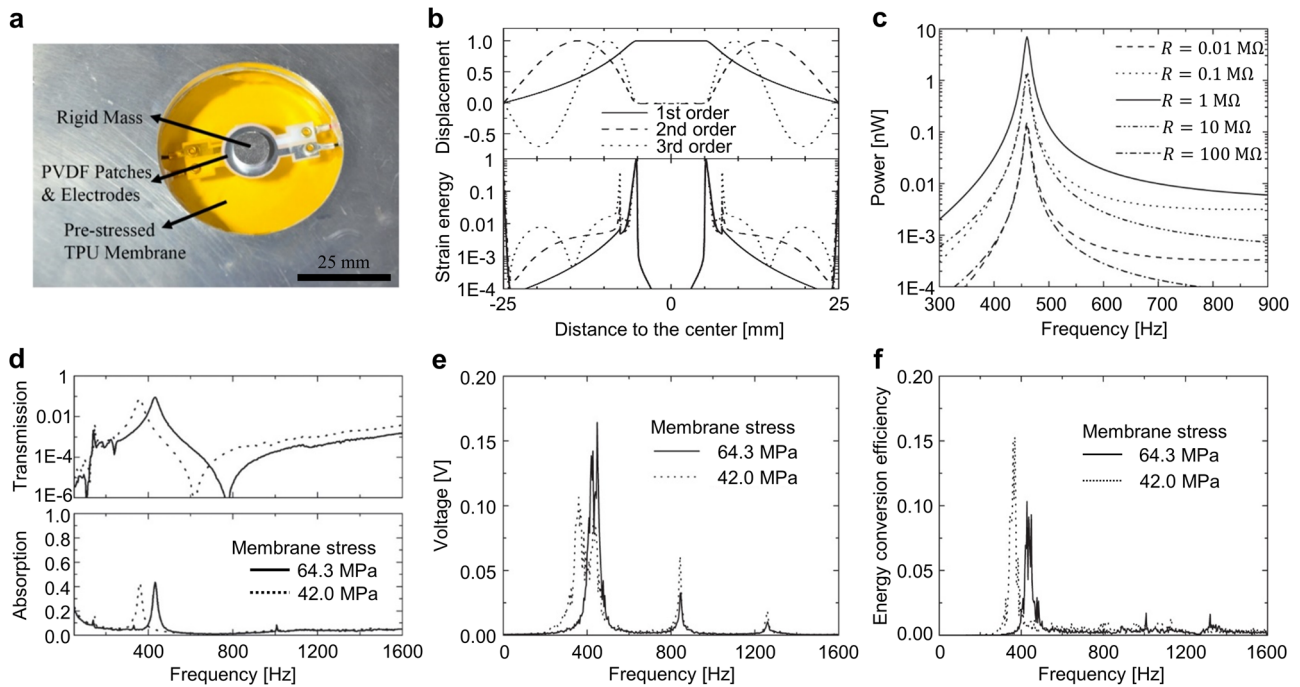


Fig. 2 Membrane-type acoustic metamaterial (MM) for energy harvesting. **a** Proposed locally resonant acoustic MM system that uses a flexible piezoelectric material (polyvinylidene fluoride film (PVDF)) and a thermoplastic polyurethane (TPU) membrane with additional mass. **b** Displacement and strain energy of the first three-order mode shapes along the central line of the MM. **c** Energy-dissipation behavior by the different resistors. The output power diminishes as the resistance increases. **d** Transmission and absorption spectra vs frequency with varying membrane stresses. **e**, **f** Output voltage and energy-conversion efficiency from acoustic MMs with different membrane stresses⁶². Reprinted with permission from ref. ⁶².

of 1 MW, and a maximum power of 0.05 mW. These values can be manipulated by changing variables such as the geometric configuration of the cantilever, the tip mass, and the piezoelectric film thickness. Remarkably, the input wave was indeed localized inside the bandgap frequency range, allowing the piezoelectric device to capture the trapped energy when wave propagation is prohibited. The energy extraction process facilitates the distribution and diffusion of energy throughout the system, hence increasing the effectiveness of vibration isolation in mechanical MMs.

Li et al.⁶² used local resonances to facilitate acoustic-to-electric energy conversion rather than vibration-to-electrical energy. A positive real-valued mass density and bulk modulus can be used to characterize acoustic wave propagation, while the use of acoustic MMs such as membrane-type resonators and Helmholtz resonators allow for the full classification of each parameter spectrum to be extended to negative and even zero values. For example, membrane-type acoustic MMs consisting of a thin membrane with one or more rigid masses attached have been shown to significantly absorb acoustic waves. Thin membrane-type MMs can achieve much stronger acoustic attenuation at the deep-subwavelength scale, compared to standard thick sound-absorbing materials. In practice, this approach provides both sound insulation and noise-based energy harvesting. This dual functionality is feasible because the local resonance strengthens the effect of the localization of energy while excluding the propagation mode. The base structure (Fig. 2a) is constructed of prestretched circular thermoplastic polyurethane, while the boundary of the membrane is attached to a rigid aluminum ring, and aluminum sheets are bonded on each side. This structure is referred to as a membrane-type acoustic MM and is well-known for its capacity to establish a negative mass density between resonant and antiresonant frequencies. For practical usage, the evolution of membrane loss contributes to lowering the efficiency

of sound insulation in the corresponding frequency range. However, this study sought to retrieve rather than dissipate the energy; i.e., to develop a MM device that is capable of both sound insulation and energy harvesting. The displacement and strain energy distribution vary along the center line of the membrane at the first three resonance frequencies (Fig. 2b). The result indicates that the strain energy of the bending deformation is largest at the central mass. Transmission-line analysis showed that the energy dissipation is maximized when the membrane and the terminated circuit have the same impedance, analogous to a capacitor and resistor (Fig. 2c). The MM sample that is subjected to each prestress on the membrane can also be used to tune the operating frequency in energy transmission and absorption spectra (Fig. 2d). When different membrane stresses (64.3 MPa and 42.0 MPa) are applied, the fundamental frequencies change (432 Hz and 356 Hz); this shift should be considered during energy conversion. The maximum voltage output is attained at the corresponding frequency where the absorption is greatest (Fig. 2e) and yields high energy-conversion efficiency (Fig. 2f).

The use of local resonators has been shown to achieve much higher PEH efficiency than the use of a conventional one, but devices consisting of a single resonator can only operate in a single frequency range. However, recent studies have shown that by using multiple resonators, PEH efficiency can be improved and devices can be designed to expand the working frequency range. Chen et al.⁶³ employed membrane-type MMs with multiple local resonators for both wave attenuation and energy harvesting in the elastic regime. This capability was achieved mainly by substantial deformation of the membrane. The proposed MM is made up of a MM beam and a pretensioned elastic membrane with a built-in split-ring mass (Fig. 3a). The MM beam has periodic holes that are filled by membrane-split ring structures. Aluminum is used for the host beam, copper for the split ring, and polyetherimide (PEI) film for the membrane. At the resonant frequency, when

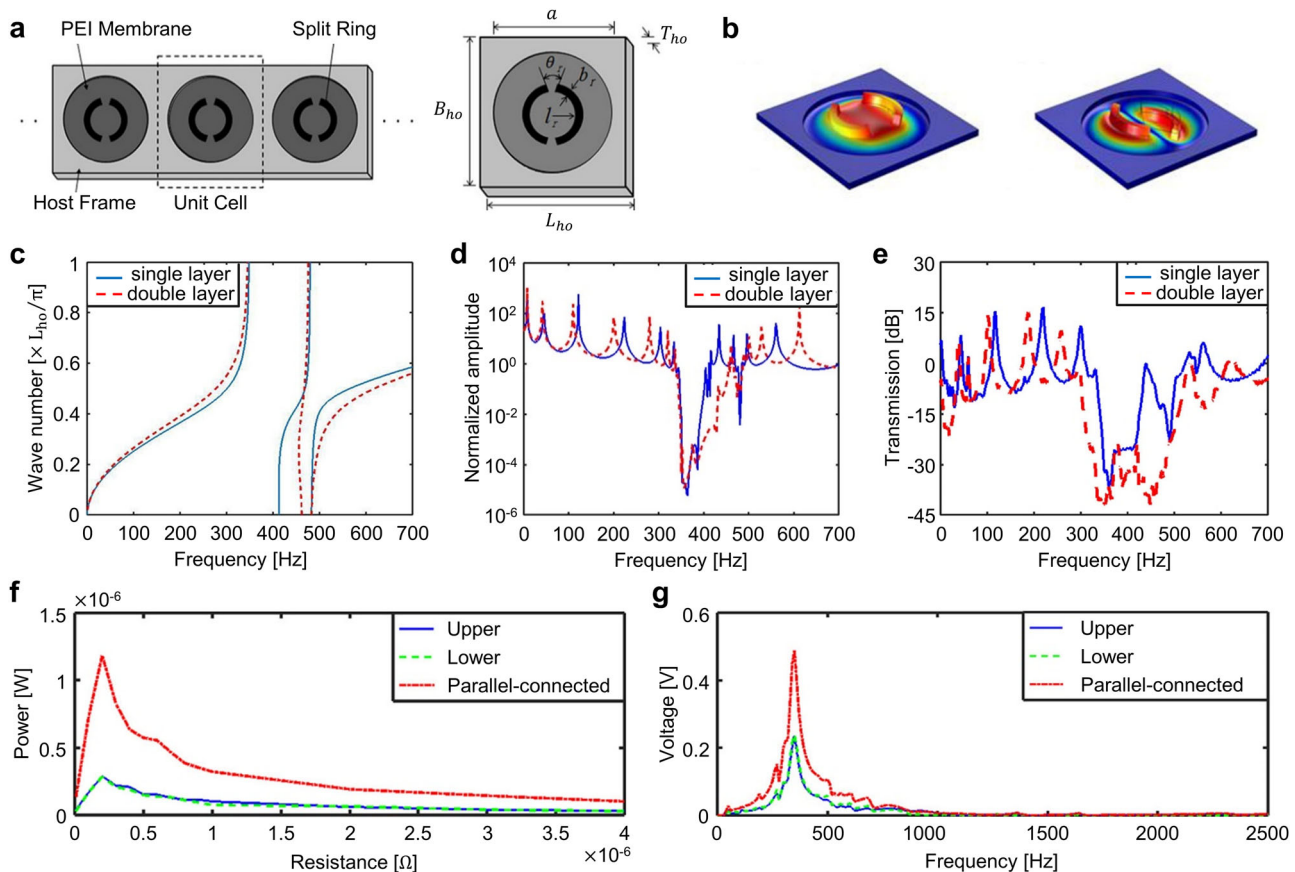


Fig. 3 Metamaterial (MM) beam with membrane-split-ring resonators for energy harvesting. **a** Configuration of a membrane-split-ring resonator embedded in a MM beam and a single unit cell. The membrane is a polyetherimide (PEI) film. **b** Mode shapes at the cutoff frequency of the first and second bandgaps. **c** Band structures of the MM beam with single- and double-layer resonators; both have two bandgaps in which the wave cannot propagate through the system. **d, e** Simulated and experimental frequency responses of the MM beam. **f, g** Output power and voltage of the MM beam with double-layer resonators⁶³. Reprinted with permission from ref. ⁶³.

the wave is severely attenuated, the voltage output reaches a maximum. The wave attenuation capable of capturing trapped energy was proved numerically, and a PVDF patch attached to the membrane could be used to convert localized energy to electrical energy. The flexural-type mode shapes of the membrane and two split rings indicate the in-phase (monopole) and out-of-phase (dipole) motions at the first and second resonant frequencies, respectively (Fig. 3b). Furthermore, a Bragg-type bandgap arises at considerably higher frequencies in the periodic assembly of the host beam, but this phenomenon is beyond the scope of their work. The corresponding band structures of the single- or double-layer MM beam reveal apparent bandgaps in which the elastic waves are highly suppressed with no real-valued wavenumber, induced by local resonances (Fig. 3c). The onset frequency of the first bandgap is broadened in a double-layer resonator made of identical resonators on the top and bottom surfaces, compared to a single-layer resonator. The single-layer structure enables estimation of two separate attenuation regions by using band-structure analysis. A major attenuation exists in the frequency range of 340–426 Hz, whereas a moderate attenuation occurs at 460–500 Hz (Fig. 3d, e). The different attenuation capabilities are mainly characterized by vibration modes. Due to the lower displacement and stress in the secondary vibration mode, the attenuation capacity is relatively looser than in the first mode that absorbs most of the external source energy. A PVDF film was mounted on the unit cell to convert vibration energy to electrical energy. For double-layer resonators (Fig. 3f), using a parallel-connected resistor rather than top and bottom

resistors demonstrated an output power four times greater than that of the single-layer structure loaded with a resistance of 200 kΩ. The output voltage peaked at 348 Hz (Fig. 3g), which is extremely close to the bandgap frequency range. The output voltage and the wave attenuation show a linear correlation, which enables the output voltage to be maximized in the first bandgap. Overall, this study provides generally consistent evidence supporting a reliable relationship between vibration mitigation and mechanical-to-electrical energy conversion.

Physical mechanism of defect modes. Defect modes are one of the wave-localization mechanisms that occur in PnCs. Bloch’s theorem states that a complete bandgap can appear in a periodic structure in which elastic or acoustic waves can no longer propagate^{64,65}. By breaking the periodicity and incorporating an impurity, a fascinating phenomenon arises in which one or more flat passbands emerge within the Bragg-induced bandgaps, so called defect modes^{66,67} (Box 1b). This method of wave localization is analogous to the localization of impurities in a semiconductor⁶⁸. By using an impurity to break the periodicity, the defect mode-induced system facilitates a flat branch in the bulk band, but a topology-induced system, particularly in the one-dimensional case, provides an interface state that can be localized by breaking the inversion symmetry^{69,70}. A defect-mode mechanism does not produce a new bandgap but has an exceptionally low slope in the dispersion curve; this trait indicates a zero group velocity, in which elastic or acoustic waves are condensed in the imperfection domain. Imperfect regions have an

independent degree of freedom at the frequency that corresponds to the defect mode, and thus can amplify the evanescent waves that surround the defect cavity. This property can be used to devise compelling PEH and the efficiency of energy harvesting can be facilitated by utilizing a piezoelectric device in the area where localized wave energy is present. Thus, by using piezoelectric materials as energy converters, the defect-mode mechanism permits the capture of localized waves. In the following subsection, we introduce state-of-the-art mechanical PEH designs that use the defect-mode mechanism to improve PEH efficiency.

PEH system using defect modes. Previous studies have attempted to improve the efficiency of PEH by using the defect mode that is induced by imperfect PnCs. Wu et al.⁷¹ demonstrated an acoustic energy harvester that uses PnCs and piezoelectric materials to trap and harvest the acoustic wave in the defect zone at the resonant frequency caused by the imperfection. Moreover, Wang et al.⁷² numerically and experimentally developed an acoustic PEH that uses curved beams in a resonant PnC cavity to localize the acoustic wave, and the output voltage and power are developed through the piezoelectric. Lv et al.⁷³ numerically and experimentally verified elastic wave energy harvesting using a two-dimensional PnC with point defect states by removing an inclusion from the periodic array, and the results showed that the energy harvesting performance of the defect cavity PnC is much higher than that of the original PnC. Chuang et al.⁷⁴ numerically and experimentally proved the feasibility of energy harvesting of defect modes by slowing down the flexural waves surrounding the defect.

However, early PEH systems had a drawback in that their working frequency was restricted to a single value. To solve this issue, Oudich et al.⁷⁵ proposed a tunable PEH to capture acoustic wave energy. This was achieved by quantifying the acoustic energy gathered by a plate with a periodic array of unit cells that contain mass-spring resonators made of impurities to produce a defect mode. Analysis of the band structure evaluated whether sound transmission loss (STL) and mechanical-to-electrical energy convergence could enable tunable acoustic energy harvesting in the low-frequency range around 500 Hz. The unit cell (Fig. 4a) consists of mass-spring resonators that are attached to a plate. Acoustic energy is confined by utilizing an imperfect plate that has a defect in the mass-spring resonators. Due to the oscillation of mass-spring resonators, the acoustic energy is transferred to mechanical energy, which is subsequently caught by piezoelectric elements and converted to electrical energy. The supercell (Fig. 4b) of the acoustic plate structure includes a defect that is obtained by removing nine resonators around the center. Band structures and STL (Fig. 4d) were analytically investigated considering Kirchhoff plate theory. The resonant frequency in this system is 950 Hz, whereas the flat mode appears in the bandgap at 1.2 kHz due to the use of the defective-cavity mode. The flat mode, which has a zero group velocity, effectively supports the desired localization. To find the optimal setting, output power and voltage were measured along with the load resistance (Fig. 4e). Compared to the existing plate, the system with nine resonators captured more acoustic wave energy and lowered the frequency range from which suitable energy could be harvested. Also, the corresponding resonant frequency (i.e., 400 Hz) is considered to further lower the bandgap around 500 Hz. Interestingly, the supercell (Fig. 4c) is composed of an impure substance rather than a geometric impurity. The stiffness of the resonators is tailored to account for imperfections in the material. The spring of resonators are rigid and only the mass effect of the plate is addressed, so the defect-induced cavity mode was generated and exploited for energy harvesting. The defect mode was created at 519 Hz, and 18.1 μW of acoustic energy was harvested

under 100 dB of acoustic pressure (Fig. 4f). When designing the mass-spring resonators on elastic substrates, the stiffness and mass must be considered. From a practical perspective, to physically model this mass-spring system, alternative structures that share the same resonance mechanisms can be considered, such as rigid materials coated or embedded with a soft medium, particularly for underwater environments⁷⁶.

Despite the great success of acoustic energy harvesting in previous proof-of-concept studies, the trapped energy is still insufficient for practical applications. Subsequently, Ma et al.⁷⁷ incorporated a MM and a Helmholtz-coupled resonator (MHCR) to increase the acoustic energy density through wave trapping and sound pressure amplification. Acoustic energy can be directed to the desired location by utilizing the defect mechanism and manipulating materials locally. For this reason, the MHCR was designed to increase the acoustic energy density surrounding the defect. The MHCR consists of a locally resonant MM plate for focusing and a Helmholtz resonator for amplification (Fig. 5a). The thin metal plate is supported by locally resonant silicone rubber pillars. In the Helmholtz resonator, a cavity and a neck are used to generate a resonance. To describe this model analytically, each pillar and Helmholtz resonator is replaced by a mass-spring model. The Helmholtz resonator, in analogy to a mass-spring equivalent system, is fabricated of silicone rubber and the substrate which is made of thin aluminum plates governed by Kirchhoff plate theory. The sound pressure is amplified by local resonance on the plate coupled to Helmholtz resonators that each have a defect. The MM plate traps the localized acoustic waves in the imperfect zone around the resonant frequencies, and subsequently, Helmholtz resonators magnify the sound pressure in cavities. The investigation of band structures of flawless supercells without taking impurities is required before implementing defect-induced MMs (Fig. 5b). The band structure that meets periodic conditions in the MM unit cell has a bandgap. However, the design process must consider the supercell configuration, which uses certain finite unit cells that have intrinsic defects. Then, by exploiting impurities to break the periodicity, defect modes (flat band) with a frequency of 2722 Hz appear in the bandgap, which correspond to the resonant frequency of the designed Helmholtz resonator. The voltage throughout the frequency response and the corresponding displacement fields were examined for the piezoelectric effect (Fig. 5c). In most frequency ranges, the MHCR generated higher voltage than the acoustic-MM (AM) that lacked the coupled resonator. The MHCR harvested 38.62 mV at the resonant frequency of 2701 Hz, which is almost double that obtained by the AM. To illustrate the structural resonance, sound pressure was stimulated and experimentally validated. The transmission spectra (Fig. 5d) derived from the voltages of the unit sound pressure of each energy harvester show that the maximum transmission of the MHCR energy harvester at 3027 Hz was up to 3.5 times more than that of the AM energy harvester. As a result, the MHCR has remarkable energy-harvesting efficiency for the target frequency of mechanical noise (2000–4000 Hz), so transmission is relatively high. The output voltage and output power (Fig. 5e) varied due to the external resistance of the MHCR energy harvester at the resonant frequency. The voltage peaks rose monotonically to an asymptote of 416.10 mV driven by the release of external resistance. At the optimal external resistance, the output power reached 23.85 μW . The MHCR is a self-powered acoustic device that can be seen as a sustainable energy transfer in the harvesting of ambient acoustic energy and is applicable to ecologically-benign energy harvesters. MHCR provides a useful pathway in designing acoustic harvesters to maximize energy density, and further improvement of perfect wave localization and harvesting capacity is feasible.

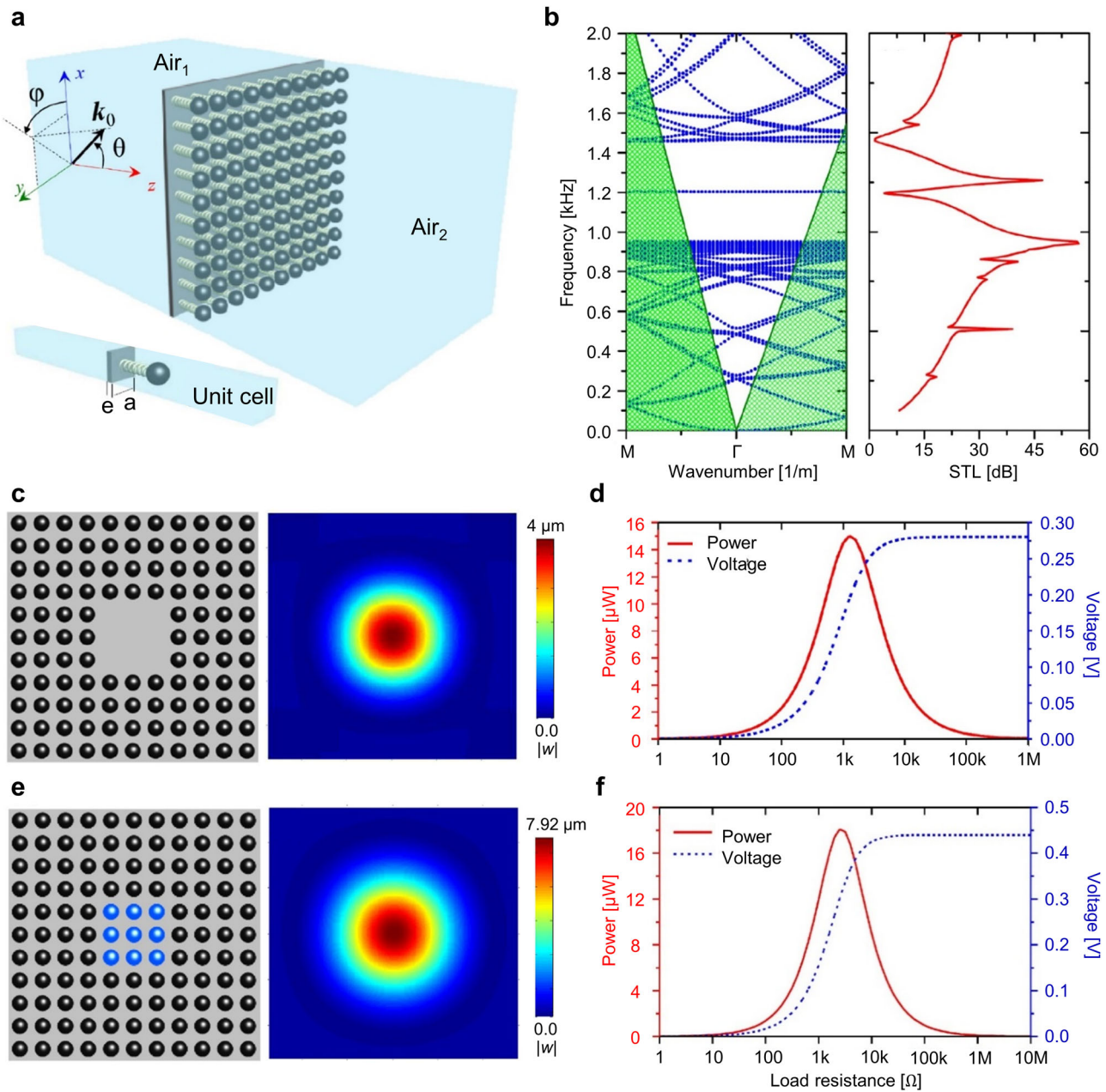


Fig. 4 Tunable subwavelength acoustic metamaterial (MM) plate for energy harvesting. **a** Simplified model of MM plate. The unit cell is composed of a spring-mass resonator and a thin plate, while the supercell MM plate is made up of a square array of unit cells; \mathbf{k}_0 : wavevector, θ : elevation, and φ : azimuth angle. Acoustic waves propagate from Air₁ to Air₂ through the MM plate. Supercell of the MM plate structure where the defect is obtained **b** by removing the nine central resonators and **c** by changing the stiffness of the nine central resonators and each displacement field of the plate at the defect mode frequency. The spring-mass resonators and stiffness changed resonators are described as black and blue spheres, respectively. **d** Calculation of the band structure and sound transmission loss (STL) about the supercell with removing nine central resonators. The edge of the green shaded region in the band structure symbolized the sound line, which determines whether airborne sounds can be radiated or not; hence, propagation modes are not permitted in the shaded region. Output power and voltage of MM plate structure **e** by removing the nine central resonators and **f** by changing the stiffness of the nine central resonators, at the frequency of the defect mode⁷⁵. Reprinted with permission from ref. ⁷⁵.

To further improve mechanical energy harvesting, several limitations should be resolved. To begin with, the currently used heuristic design approaches should be interchanged with more systematic selection rules using established using methods such as stochastic design or deep learning for inverse design, with the results being verified experimentally. Second, although the demonstrations shown so far show the feasibility of energy harvesting, the power is still bounded to sub-micro watts. Park et al.⁷⁸ obtained a significant increase in mechanical PEH using

defective frameworks of octagonal PnCs that give rise to high energy density. The design was theoretically optimized to increase the bandgap width, and was proved experimentally. The proposed unit cell consists of an octagonal hole punched into a square plate (Fig. 6a). This highly anisotropic unit cell provides numerous degrees of freedom for structural parameters to be optimized, and therefore the unit cell can be adjusted to tune the bandgap. The geometry was optimized using an objective function based on the width of the bandgap, especially at the target frequency of 50 kHz.

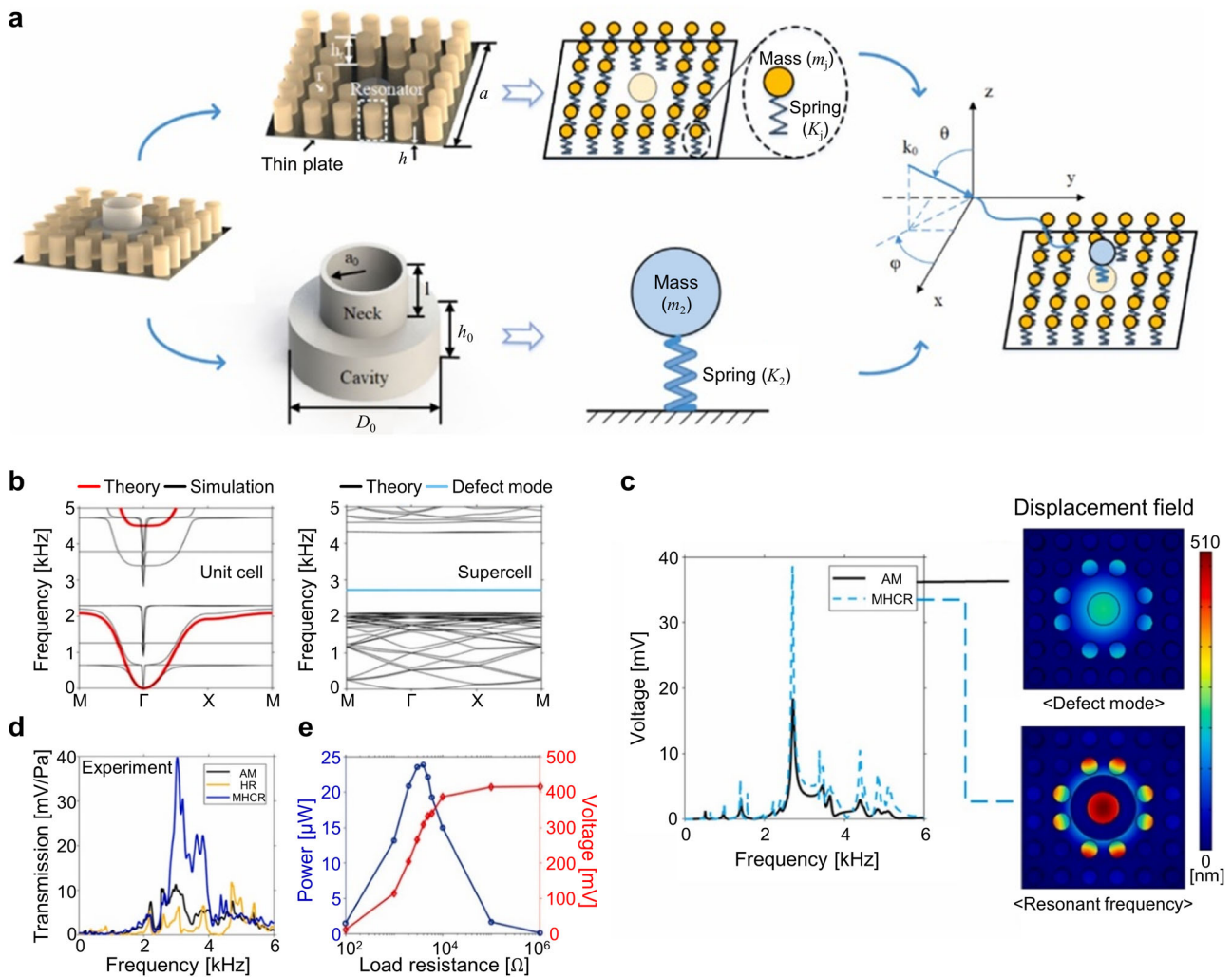


Fig. 5 Metamaterial and Helmholtz-coupled resonator (MHCR) for energy harvesting. **a** Theoretical model of the MHCR; each resonator and Helmholtz resonator (HR) element is represented by a mass-spring resonator. **b** Band structures of the unit cell in theory and numerical simulation, and the band structure of the supercell in theory. Both band structures, theoretically, have the same bandgap frequency range, which prevents the acoustic wave from propagating. **c** Simulated output voltage of acoustic-metamaterial (AM) and MHCR, and displacement field of AM in defect mode and MHCR in resonant mode. **d** Experiment results of transmission per frequency for each resonator plate. **e** Output power and voltage per resistance of the MHCR⁷⁷. Reprinted with permission from ref. 77.

Any material can be used for PnCs in a host-inclusion system unless they have an indistinguishable impedance contrast in terms of mass density or elastic modulus. The optimal design demonstrates a bandgap spanning from 46.93 kHz to 52.68 kHz, with a central frequency of 49.80 kHz, extremely close to the target frequency of 50 kHz (Fig. 6b). The complete bandgap across the high-symmetry lines ensures that waves cannot propagate in any direction into the PnC structure at the corresponding frequencies. In this case, the optimized octagonal unit cell has a broader bandgap frequency range than the commonly-investigated configuration, i.e., the circular structure. Moreover, the proposed unit cell has a lattice constant smaller than that of circular one, allowing for a denser design. The bandgap propagation dynamics facilitates reflection of all energy, leaving just the local evanescent wave within the PnCs due to displacement continuity. A defect mode was established by removing a single unit cell from the area in which displacement fields are localized (Fig. 6c). Harmonic analysis verified the bandgap effect of the supercell of the defect-based PnC. Numerical findings of displacement fields revealed highly-attenuated waves throughout the entire system, but well-preserved localized waves at the defect did not violate energy conservation. A

significant reduction in wave amplitude after the second column indicates that elastic wave energy is confined to this layer, and provides a potential source of energy generation by the use of defects. The output voltage over electrical resistance was much higher on MM plates than on bare plates (Fig. 6d), and gave a dramatic increase in voltage at low resistance. This voltage rapidly converges to a steady state, the existence of this state implies that the electrical-impedance matching condition has been satisfied and is thus immune to any perturbation during elastic energy harvesting using piezoelectric devices. Moreover, the reported output voltages indicated that the MM plates generated much more power than the bare plates (Fig. 6e), and that the amplification ratio reaches its maximum of 22.8. The displacement distribution over frequency (Fig. 6f) confirmed that the presence of a PEH device did not change the target frequency, but did slightly reduce the amplitude of displacement fields, despite the device remaining functional for energy harvesting.

Physical mechanism of GRIN systems. Wave-localization phenomena that exploit local resonances suffer from being severely

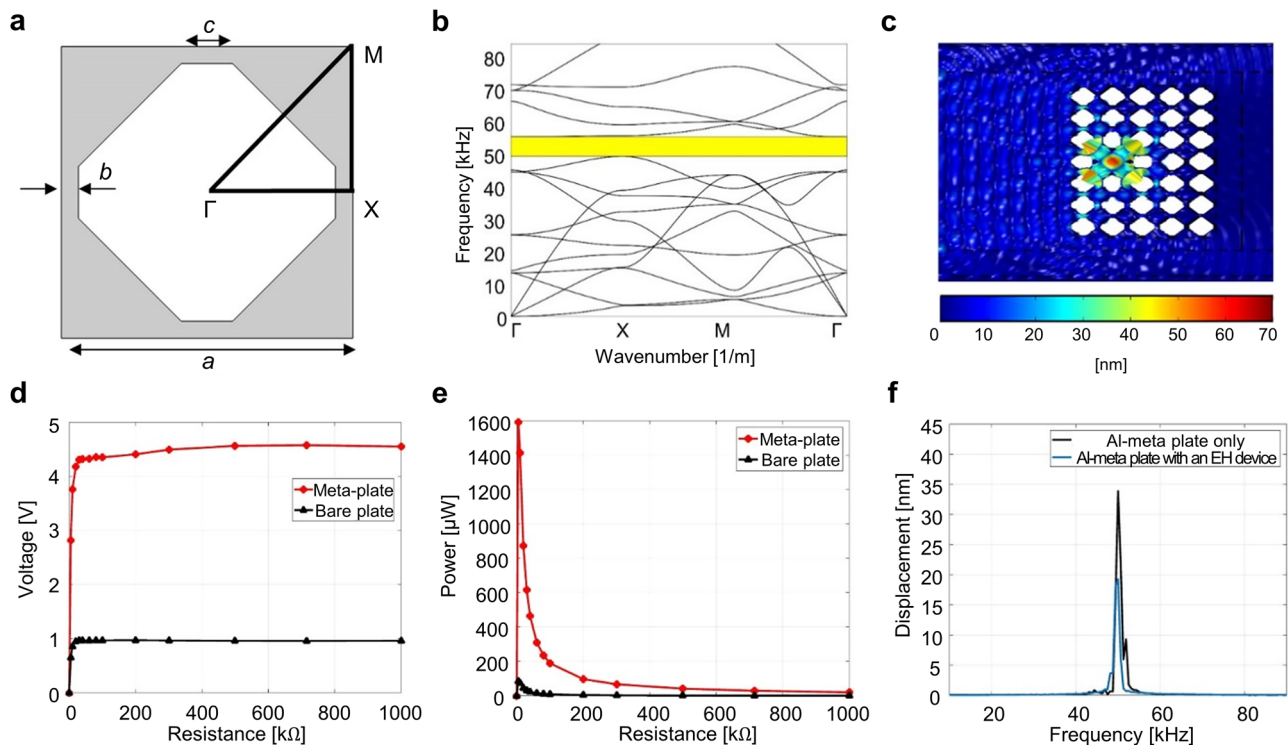


Fig. 6 Two-dimensional octagonal phononic crystals (PnCs) for energy localization and harvesting. **a** Unit cells of two-dimensional octagonal PnCs, a , b , and c , determine the geometric parameters. **b** Band structure of the unit cell calculated using the first irreducible Brillouin zone (Γ -X-M- Γ). The yellow area represents a bandgap across which the elastic wave cannot propagate. **c** Simulation results of energy localization at the defect of the PnC supercell structure. **d**, **e** Output voltage and power per resistance in the metamaterial (MM) plate and the bare plate. **f** Displacement vs frequency obtained by fast Fourier transform (FFT) for the Al MM plate with and without an energy-harvesting device⁷⁸. Reprinted with permission from ref. 78.

restricted to a particular frequency range. To overcome this, mechanical wave guiding and focusing strategies spawned by optical-transformation devices have been developed^{79,80}. To control the propagation of elastic or acoustic waves, the refractive index of each unit cell is modulated gradually in line with its density and elastic modulus (Box 1c). The refractive index of the medium is gradually customized to guide waves in GRIN structures; the customization is often used by a non-dispersive feature that provides a broadband operating frequency. Such a GRIN system may be classified as using either MMs or PnCs as elements. They could be thought of as MMs that use non-resonant elements at the subwavelength scale, and the constitutive non-dispersive wave parameters can be extracted using the S-parameter retrieval method or homogenization theory^{81,82}. GRIN systems could also be considered PnCs for obtaining gradient indices from band structures, particularly in the non-dispersive regime far below Bragg gap frequencies, by averaging wavevector information. We provide some examples of GRIN lenses that can be used for energy harvesting by inducing a focal point with gradient refractive indices. The most straightforward configuration of the GRIN profile^{83,84} is to use a refractive-index profile as a function of a hyperbolic secant formula in the transverse (y) direction given by, $n(y) = n_0 \operatorname{sech}(\alpha y)$, where n_0 is the background refractive index and α is the gradient coefficient. This gradient is extensively used for focusing and collimation in planar waveguides. According to the formula, the gradient refractive index bends rays or waves toward a focal point on the central axis by redirecting the wave along the propagation axis. Ray trajectories across the GRIN medium describe the focal length, $f = \pi/(2\alpha)$, which can be controlled by altering the filling fraction or elastic properties of each inclusion. The focal point is where the wave energy is steered and concentrated, so this system

could also be utilized to convert wave energy to electrical energy by using a mechanical-wave transducer strategically placed there.

PEH systems using GRIN systems. Numerous designs using PnCs with variable refractive indices can guide and focus mechanical waves. Tol et al.^{85–87} proposed the use of a GRIN PnC lens to significantly amplify elastic waves during PEH. The modulation of the inclusion of each unit cell in a GRIN structure with a gradient refractive index yielded the generation of Lamb waves. Subsequently, the same group⁸⁸ developed a Luneburg lens to improve the efficiency of the focusing capability of both unidirectional and omnidirectional waves. Moreover, Zareei et al.⁸⁹ designed a continuous profile flexural GRIN lens by varying the thickness of the plate rather than the inclusion parameters. Recent years have seen the emergence of more efficient GRIN-based focusing PnC structures for elastic or acoustic waves through a variety of approaches, incorporating optimization and advanced 3D printing techniques.

Hyun et al.⁹⁰ investigated an elastic GRIN lens that conveys flexural waves to a desired focal point, 2D PnCs embedded in a plate, and is particularly well-suited for the high-frequency range, where the presence of shear deformation is no longer negligible. The PnC design was optimized using a genetic algorithm. The shape of the unit cell was determined by the lattice constant and the hole radius (Fig. 7a). The wavelength of the first flexural wave mode was adjusted to ~ 19.2 mm by setting the target frequency of the aluminum plate to 50 kHz. To satisfy the homogenization limit, lattice constant $a = 5$ mm was selected as it is approximately a quarter of the wavelength. The GRIN lens was constructed as an array of unit cells with optimum radii (Fig. 7b). The band structure (Fig. 7c) was computed using the standard Galerkin method with discretized governing equations. The

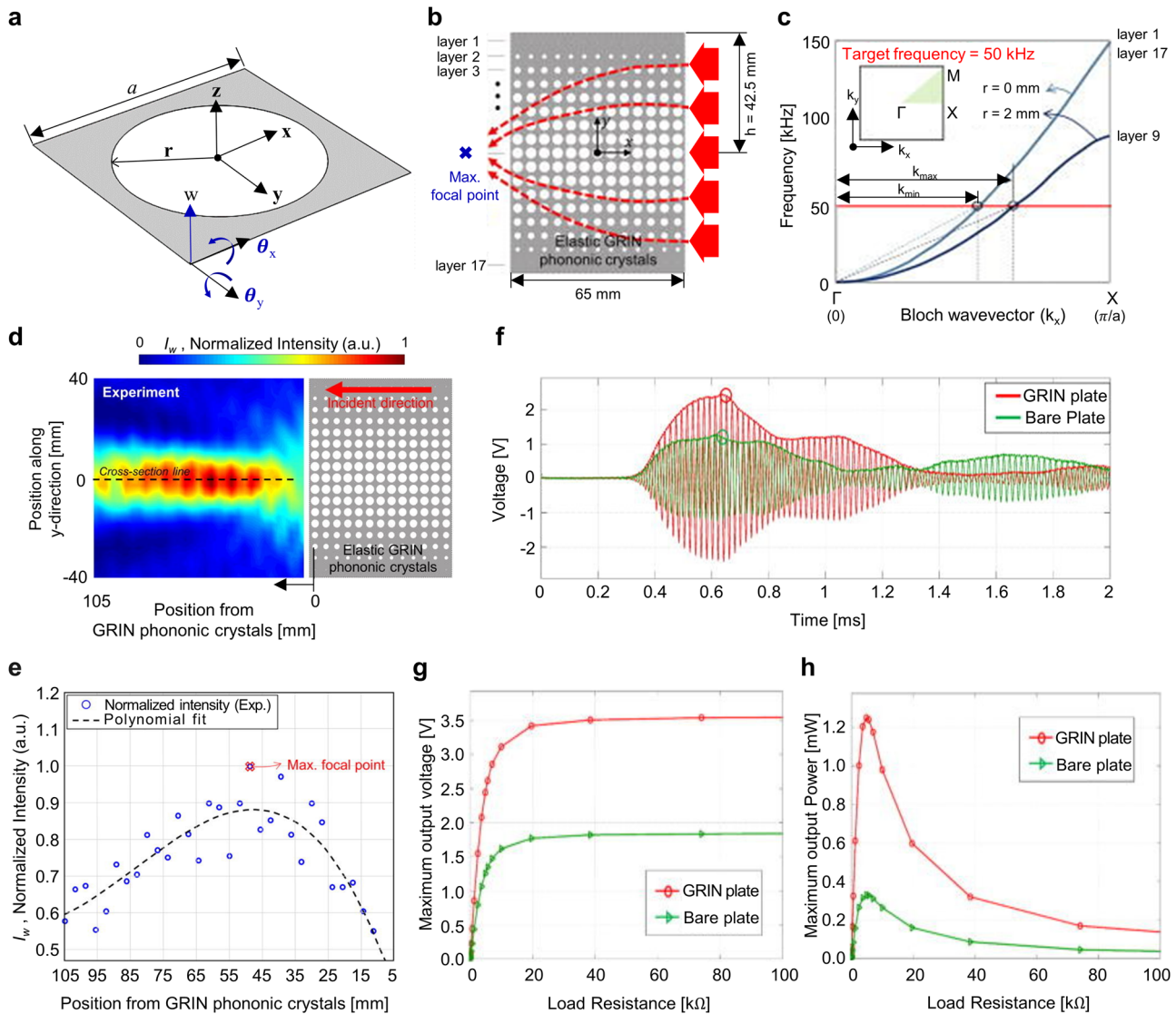


Fig. 7 Gradient-index (GRIN) lens for focusing and harvesting flexural wave energy. **a** Unit cell of 2D GRIN lens for Reissner-Mindlin plate with lattice constant a and hole radius r ; $x, y,$ and z : Cartesian coordinates; w : transverse displacement, θ_x : x -rotational angle, θ_y : y -rotational angle of flexural wave. **b** GRIN lens arranged by changing r to focus the flexural wave at the calculated focal point. The incident plane wave is excited from left to right. **c** Band structure of the unit cell calculated by the first irreducible Brillouin zone (Γ -X-M- Γ) with the maximum and minimum radius of the hole. Red line: target frequency of 50 kHz. **d, e** Normalized intensity distribution of transverse displacement, and cross-sectional plot along the central axis measured experimentally. **f** Output voltage distribution by time-domain analysis measured at load resistance 4.8 kW. Maximum output of energy harvesting of **g** voltage and **h** power at various load resistances⁹⁰. Reprinted with permission from ref. ⁹⁰.

radius of the unit cell varied along the radius, so the velocity of the flexural wave decreases as the refractive index increases. Consequently, by Snell’s law, the path of the wave is gradually shifted toward the focal point. To experimentally verify the optimized GRIN lens, the designed GRIN plate was fabricated by drilling a hole in the aluminum plate. A piezoelectric element was attached to the analytically obtained focal point to validate the energy harvesting capability. By using transverse displacement fields, the normalized intensity I_w along the position was obtained (Fig. 7d). The intensity was normalized over the position along the cross-section (Fig. 7e), and to achieve the largest efficiency at the optimal position, the focal point was found by searching for the location at which the normalized intensity was closest to 1.0. This is the position of wave localization, and can be used for energy harvesting by attaching piezoelectric devices. The normalized intensity was high over a wide range around 40 mm, so other preferences with respect to focal spots of energy harvesting are

available. The output voltage-response waveform (Fig. 7f) was measured at the maximum focal point of the GRIN plate and the bare plate. The focusing effect of the GRIN plate resulted in an output voltage approximately double of the bare plate. The maximum output voltage over load resistance for both plates (Fig. 7g) showed an abrupt change at low resistance, and gradually converged. The maximum output power over load resistance for both plates was about twice that of the bare plate (Fig. 7h), in agreement with the previous result. Consequently, the GRIN energy-harvesting system is compact, so power generation can be compact. The system also offers directional control, so the user can concentrate elastic energy towards the desired focal point.

With the development of 3D printing techniques capable of fabricating complex geometries at the macroscale, Tol et al.⁹¹ recently developed a 3D-printed PnC lens to steer and harvest elastic waves. In an index parametric manner, a bilayer 3D-

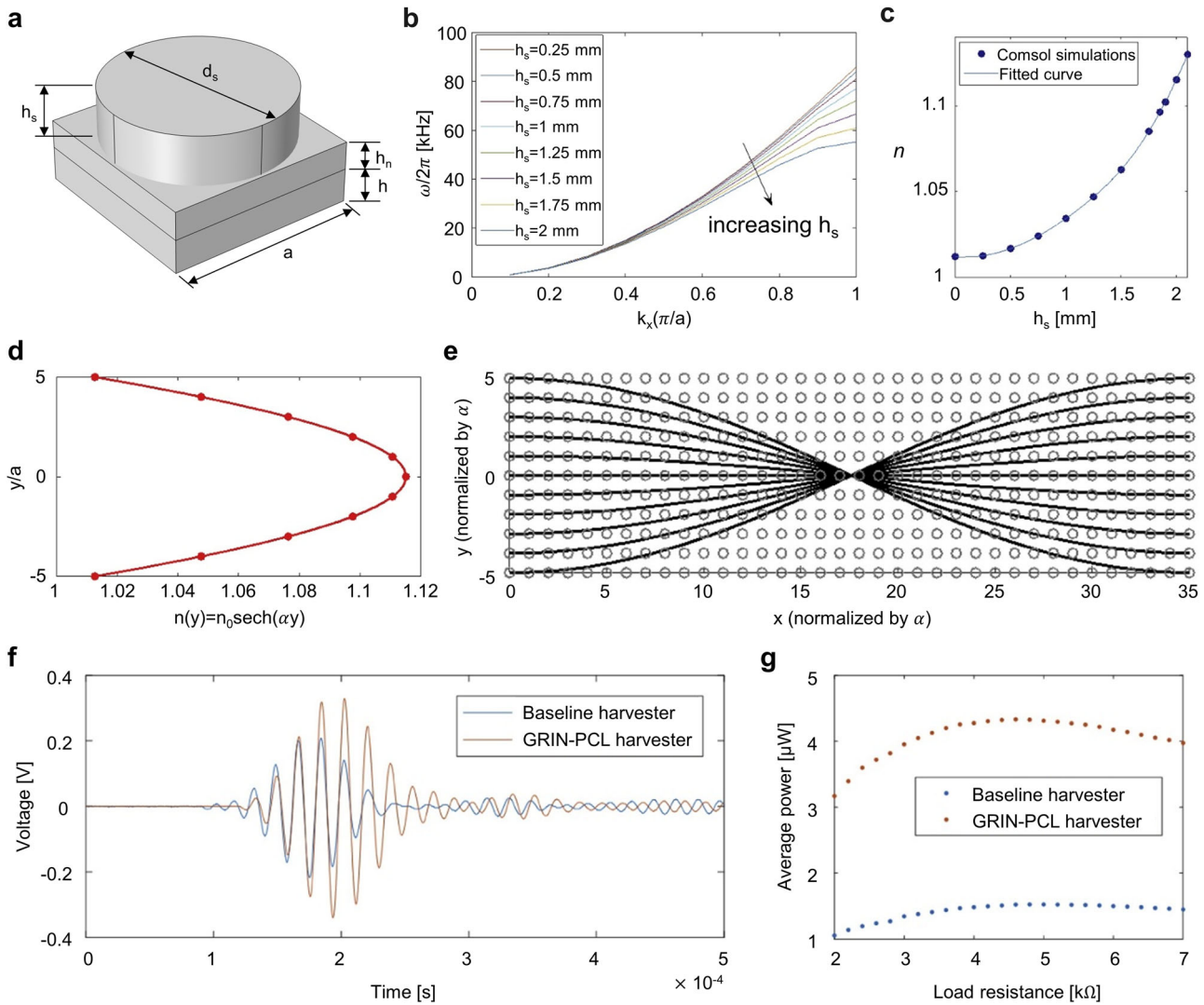


Fig. 8 3D-printed gradient-index (GRIN) lens for elastic wave focusing and energy harvesting. **a** Unit cell composed of heterogeneous materials. **b** Band structure of the lowest extensional Lamb wave along the x -direction with varying stub heights. **c** Refractive index of the unit cell as it varies with stub height. **d** Hyperbolic secant distribution of the refractive-index profile and **e** beam trajectory obtained from the same profile analytically. **f, g** Energy harvesting: Output voltage per time and average power per load resistance with and without a GRIN-phononic crystal lens (GRIN-PCL)⁹¹. Reprinted with permission from ref. ⁹¹.

printed GRIN lens made of a host aluminum plate with an array of nylon stubs was designed. The height of the stubs at the bottom of the base plate determine the corresponding refractive index profile, which follows a hyperbolic secant gradient distribution for the lowest antisymmetric mode (A0) of Lamb waves in the band structure (Fig. 8b). The 3D-printed GRIN lens was designed by establishing a relationship between the height of the stubs and the refractive index of the unit cells (Fig. 8c) to fulfill the hyperbolic secant GRIN distribution at 40 kHz (Fig. 8d). The transition from non-dispersive to dispersive characteristics is dependent on the height and is balanced at the bandgap at around 55 kHz, while the maximum and minimum heights were determined with consideration of the resolution of the 3D printer. According to the ray tracing approach, the first focal point appears at a position of 17.6 times of the lattice constant a (Fig. 8e). Time-domain numerical simulations were undertaken to obtain the out-of-plane velocity field and illustrated the wave-focusing effect of the 3D-printed GRIN lens. The excited plane waves converged to the focal point at which the refractive index was highest (equivalently,

the wave velocity was slowest), then re-diverged while propagating through the GRIN medium. In the experimental demonstration, eighteen piezoelectric transducers were mounted on an aluminum plate to produce a plane-wave envelope following the Huygens-Fresnel principle. The output voltage was measured over time for the GRIN lens with a load resistance of 4.6 kΩ and a reference plate with a load resistance of 4.8 kΩ (Fig. 8f). The GRIN lens harvester improved the output power by up to 2.84 times (Fig. 8g).

The GRIN phenomenon can also be used to focus acoustic waves that can be harvested. Allam et al.⁹² designed a 3D acoustic lens for the audible frequency range (20 Hz–20 kHz) to increase output voltage and power by using piezoelectric devices. The unit cell was composed of a 3D-printed cross-shaped polymer in air. The effective speed of sound ($c_{\text{eff}} = 2\pi f/k$, where f is the frequency and k is the wavenumber) has a slope in the band structure and can be modulated by adjusting the volume-filling fraction (Fig. 9a). The effective speed of sound also defines the effective refractive index, $n_{\text{eff}} = c_{\text{air}}/c_{\text{eff}}$. This relationship was used to design the GRIN lens to

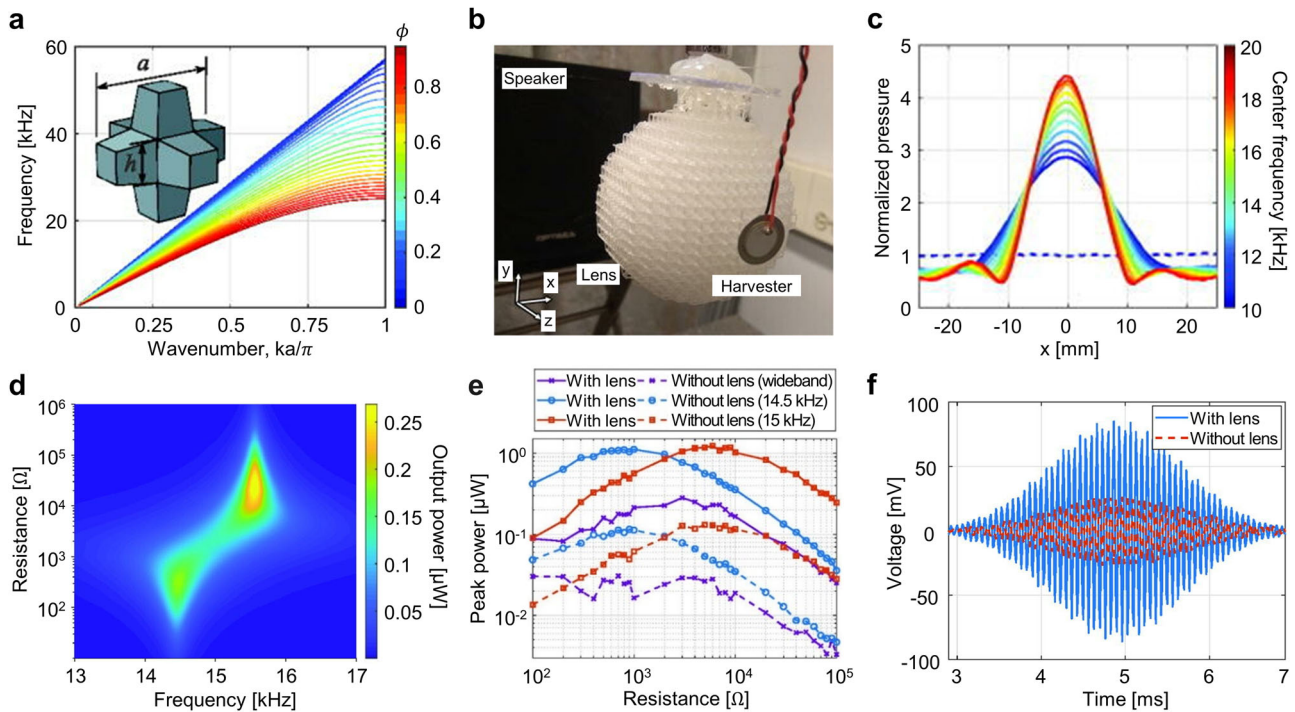


Fig. 9 3D-printed gradient-index (GRIN) lens for harvesting acoustic energy. **a** Unit cell and its band structure along the main direction of wave propagation for various volume-filling fractions, $\phi = (3ah^2 - 2h^3)/a^3$, where a is the lattice constant and h is the height of part of the unit cell depicted in figure. **b** Experimental setup to measure energy harvesting by piezoelectric devices. **c** Normalized pressure at different central frequencies, with a constant bandwidth of 6 kHz. **d** Output power vs frequency and resistance for a uniform harmonic pressure of 30 Pa. **e** Experimentally harvested peak power per resistance for an incident acoustic plane wave with a pressure of 30 Pa. **f** Numerical result of output voltage time series for maximum power output with and without GRIN lens⁹². Reprinted with permission from ref. ⁹².

have a Luneburg profile $n(r) = \sqrt{2 - (r/R)^2}$, where r is the radial distance from the origin and R is the radius of the lens. The Luneburg profile enables rays or waves to be perfectly focused at a single point on the opposite side of the lens without aberration. The analytic profile of the refractive index was used to design a 3D spherical GRIN lens composed of ten unit cells (Fig. 9b). The unit cells may seem to have anisotropic properties due to their non-symmetric shape, but by adopting a low frequency range with a nondispersive feature, the effective properties become isotropic, so the components can be easily fabricated to be compact. The normalized pressure over position (Fig. 9c) can be increased at the focal point, and the lens works in a broad frequency range. Piezoelectric elements were mounted at the estimated focal point to experimentally validate the 3D GRIN lens's energy harvesting capability. The output power was obtained by varying the frequency and resistance while maintaining a uniform harmonic pressure of 30 Pa (Fig. 9d). The peak at 14.5 kHz corresponds to a short-circuit resonance, but the peak at 15.5 kHz corresponds to an open-circuit resonance. The center frequencies and bandwidth varied according to the bandwidth and the presence or absence of a lens (Fig. 9e). The GRIN lens significantly increased the power supplied to the resistance. The voltage over time (Fig. 9f) reveals that the presence of the GRIN lens expanded the voltage bandwidth substantially. Consequently, a GRIN lens specialized to concentrate audible acoustic waves can be used as an energy harvester, and can increase the output voltage and power to the load by more than an order of magnitude than without the use of a GRIN lens.

Outlook

We have presented an overview of various early modern piezoelectric energy harvesters that use designed artificial mechanical

structures (i.e., MMs and PnCs) to produce wave localization or focusing mechanisms by exploiting local resonance, defect mode, and GRIN systems. The PEH capabilities of these methods are summarized in Table 1, where the output voltage and power of each system, according to their geometrical dimensions, local resistance, and target frequency are compared. Despite exhibiting PEH efficiency, all examples have more efficient harvesting performances than conventional energy harvesters. The PEH response of each mechanism has its own distinctive features, which can be described by the pros and cons of each underlying principle. First, owing to the bandgap induced by local resonances, PEH using local resonators can operate at relatively low-frequencies, and extremely high-density energy confinement can be achieved. Furthermore, the operating frequency range can be tuned at will through the design of the resonator. However, the working frequency range is limited to a relatively narrow band. Secondly, PEH using defect modes exploit Bragg-type bandgaps, allowing them to operate in a higher frequency range than using local resonances. One or more defect modes are established within the bandgap, depending on the eigenmode of the impurity contained inside the periodic structure, so efficient PEH working at different frequencies can be realized. The defect-mode mechanism exploits the resonance of independent degrees of freedom of the impurity, and therefore achieves a very high density of energy localization. Similarly, this method operates in a narrow frequency range, and the calculation of the defect modes in band structures is a fairly time consuming and difficult task. In certain cases, an analytic derivation^{93,94} is used to determine the defect mode, although its universal implementation is limited. Third, GRIN-based wave localization PEH function over a larger frequency range, but it provides a lower PEH efficiency. Also, multiple unit cells with a gradual variation should be arranged, so

Table 1 Summary of mechanical energy harvesters that use mechanical metamaterials or phononic crystals.

Harvesting Mechanism	Subject	Unit Cell Size [mm ³]	Sound Pressure Level [dB]	Load Resistance [Ω]	Resonant Frequency [Hz]	Output Voltage [V]	Output Power [μ W]
Local Resonance	Locally resonant cantilever mechanical metamaterial ⁶¹	35 × 35 × 1	Elastic wave	1 × 10 ⁶	170	0.22	0.05
	Membrane-type acoustic metamaterial ⁶²	$\pi (25)^2(2)$	20	1 × 10 ⁶	432	0.17	0.03
	Metamaterial beam with membrane-splitting resonator ⁶³	45 × 45 × 2	Elastic wave	0.2 × 10 ⁶	348	0.5	1.25
Defect Mode	Tunable sub-wavelength acoustic metamaterial plate ⁷⁵	110 × 110 × 0.5	100	2511.9	519	0.44	18.1
	Metamaterial and Helmholtz coupled resonator ⁷⁷	60 × 60 × 16.4	114	4000	3027	0.53	93.13
	Two-dimensional octagonal phononic crystals ⁷⁸	169 × 236.6 × 2	Elastic wave	4990	49800	4.55	1590
GRIN	GRIN lens for flexural wave ⁹⁰	65 × 85 × 2	Elastic wave	4800	50000	3.57	1250
	3D-printed GRIN lens for elastic wave ⁹¹	175 × 55 × 1	Elastic wave	4600	55000	0.33	4.4
	3D-printed GRIN lens for acoustic ⁹²	$(4\pi(30)^3)/3$	120	6000	15000	0.08	1.2

the system becomes relatively bulky. By weighing up these unique features, the most appropriate mechanism can be identified for the given purpose.

These PEH structures have the potential to be applicable to wireless communication or small electronic devices, but further research is required to increase the harvested voltage and power. Several alternatives have been presented to solve the shortcomings of these mechanisms, alongside breaking the limitations of current PEH devices. For example, PEH with multiple resonators⁹⁵ is being explored to overcome the limitation of local the single working frequency of PEH that uses resonance. Similarly, the constructive effect of multiple impurities⁹⁶ on PEH in defect modes is being investigated. Furthermore, rather than just localizing or focusing on the mechanical waves, the efficiency of PEH could be improved by raising the ratio of energy converted from the piezoelectric device. Therefore, by designing MM or PnC with the dielectric material used in piezoelectric devices, high-efficiency PEH may be achieved by minimizing the phase difference caused by the impedance mismatch^{76,97}.

Combinations of the mechanisms discussed in this Review is a potential topic of future research to increase the efficiency of PEH. For example, if the GRIN structure is used to focus mechanical waves, a functional and efficient PEH may be developed by inserting a defect cavity or local resonator in the focusing area. Another way to realize PEH across a broad frequency range is to build a system that has a bandgap induced by local resonance and Bragg-scattering concurrently, such as a structure with a local resonator and a defect cavity. These strategies will require development of ways to control the mechanisms that operate in different frequency spectra.

More recently, studies on PEH have been undertaken to employ mechanisms other than the local resonances, defect modes, and GRIN mechanisms as discussed in this Review. One example is wave localization in edge/interface modes using topological MMs^{98,99}. The use of topological features has the

privilege of being incredibly robust against undesirable defects. Furthermore, although all of the systems addressed here operate in the linear domain, wave localization effects in the nonlinear domain^{100,101} will also be an excellent candidate for improving PEH efficiency.

The output voltage and power produced by piezoelectric materials and devices in various PEH methods are determined by the material, size, and arrangement in periodic unit cells or local structures. The primary strength of the present studies on MM-enabled energy harvesting is in the amplification of the energy of the input mechanical wave, to achieve tens to hundreds of times greater voltages and power output than conventional materials can provide. As a consequence of these findings, renewable and ecologically-benign energy sources will be extensively utilized in next-generation electronics.

Data availability

No data sets were generated or analyzed during the current study.

Received: 6 June 2021; Accepted: 23 March 2022;

Published online: 19 April 2022

References

1. Erturk, A. & Inman, D. J. Piezoelectric energy harvesting. *John Wiley & Sons* (2011).
2. Kim, H. S., Kim, J.-H. & Kim, J. A review of piezoelectric energy harvesting based on vibration. *Int. J. Precis. Eng. Manuf.* **12**, 1129–1141 (2011).
3. Whatmore, R. Pyroelectric devices and materials. *Rep. Prog. Phys.* **49**, 1335 (1986).
4. Bowen, C. R. et al. Pyroelectric materials and devices for energy harvesting applications. *Energy Environ. Sci.* **7**, 3836–3856 (2014).
5. Neville, R. C. Solar energy conversion: the solar cell. *Elsevier* (1995).
6. Fonash, S. Solar cell device physics. *Elsevier* (2012).
7. Jaffe, H. Piezoelectric ceramics. *J. Am. Ceram. Soc.* **41**, 494–498 (1958).
8. Veselago, V. G. Electrodynamics of substances with simultaneously negative electrical and magnetic permeabilities. *Usp. fiz. nauk* **92**, 517–526 (1967).

9. Pendry, J. B. Negative refraction makes a perfect lens. *Phys. Rev. Lett.* **85**, 3966 (2000).
10. Pendry, J. B., Schurig, D. & Smith, D. R. Controlling electromagnetic fields. *Science* **312**, 1780–1782 (2006).
11. Smith, D. R., Pendry, J. B. & Wiltshire, M. C. Metamaterials and negative refractive index. *Science* **305**, 788–792 (2004).
12. Lee, S. H., Park, C. M., Seo, Y. M., Wang, Z. G. & Kim, C. K. Acoustic metamaterial with negative modulus. *J. Phys.: Condens. Matter* **21**, 175704 (2009).
13. Li, J. & Chan, C. T. Double-negative acoustic metamaterial. *Phys. Rev. E* **70**, 055602 (2004).
14. Sui, N. et al. A lightweight yet sound-proof honeycomb acoustic metamaterial. *Appl. Phys. Lett.* **106**, 171905 (2015).
15. Yang, Z., Mei, J., Yang, M., Chan, N. & Sheng, P. Membrane-type acoustic metamaterial with negative dynamic mass. *Phys. Rev. Lett.* **101**, 204301 (2008).
16. Lee, D., Nguyen, D. M. & Rho, J. Acoustic wave science realized by metamaterials. *Nano convergence* **4**, 1–15 (2017).
17. Wu, Y., Lai, Y. & Zhang, Z.-Q. Elastic metamaterials with simultaneously negative effective shear modulus and mass density. *Phys. Rev. Lett.* **107**, 105506 (2011).
18. Kim, E. et al. Highly nonlinear wave propagation in elastic woodpile periodic structures. *Phys. Rev. Lett.* **114**, 118002 (2015).
19. Park, J., Lee, D. & Rho, J. Recent advances in non-traditional elastic wave manipulation by macroscopic artificial structures. *Appl. Sci.* **10**, 547 (2020).
20. Zhu, R., Liu, X., Hu, G., Sun, C. & Huang, G. Negative refraction of elastic waves at the deep-subwavelength scale in a single-phase metamaterial. *Nat. Commun.* **5**, 1–8 (2014).
21. Colombi, A., Colquitt, D., Roux, P., Guenneau, S. & Craster, R. V. A seismic metamaterial: The resonant metawedge. *Sci. Rep.* **6**, 1–6 (2016).
22. Colombi, A., Roux, P., Guenneau, S., Gueguen, P. & Craster, R. V. Forests as a natural seismic metamaterial: Rayleigh wave bandgaps induced by local resonances. *Sci. Rep.* **6**, 1–7 (2016).
23. Milton, G. W. & Willis, J. R. On modifications of Newton's second law and linear continuum elastodynamics. *Proc. R. Soc. A: Math., Phys. Eng. Sci.* **463**, 855–880 (2007).
24. Yao, S., Zhou, X. & Hu, G. Experimental study on negative effective mass in a 1D mass-spring system. *N. J. Phys.* **10**, 043020 (2008).
25. Fang, N. et al. Ultrasonic metamaterials with negative modulus. *Nat. Mater.* **5**, 452–456 (2006).
26. Wells, B. M., Zayats, A. V. & Podolskiy, V. A. Nonlocal optics of plasmonic nanowire metamaterials. *Phys. Rev. B* **89**, 035111 (2014).
27. Orlov, A. A., Voroshilov, P. M., Belov, P. A. & Kivshar, Y. S. Engineered optical nonlocality in nanostructured metamaterials. *Phys. Rev. B* **84**, 045424 (2011).
28. Wurtz, G. A. et al. Designed ultrafast optical nonlinearity in a plasmonic nanorod metamaterial enhanced by nonlocality. *Nat. Nanotechnol.* **6**, 107–111 (2011).
29. Ghatak, A., Brandenbourger, M., van Wezel, J. & Coulais, C. Observation of non-Hermitian topology and its bulk-edge correspondence in an active mechanical metamaterial. *Proc. Natl Acad. Sci.* **117**, 29561–29568 (2020).
30. Coppolaro, M. et al. Extreme-parameter non-Hermitian dielectric metamaterials. *ACS Photonics* **7**, 2578–2588 (2020).
31. Zhou, D. & Zhang, J. Non-hermitian topological metamaterials with odd elasticity. *Phys. Rev. Res.* **2**, 023173 (2020).
32. Huber, S. D. Topological mechanics. *Nat. Phys.* **12**, 621–623 (2016).
33. Nash, L. M. et al. Topological mechanics of gyroscopic metamaterials. *Proc. Natl Acad. Sci.* **112**, 14495–14500 (2015).
34. Yu, K., Guo, Z., Jiang, H. & Chen, H. Loss-induced topological transition of dispersion in metamaterials. *J. Appl. Phys.* **119**, 203102 (2016).
35. Quan, L., Ra'di, Y., Sounas, D. L. & Alù, A. Maximum Willis coupling in acoustic scatterers. *Phys. Rev. Lett.* **120**, 254301 (2018).
36. Melnikov, A. et al. Acoustic meta-atom with experimentally verified maximum Willis coupling. *Nat. Commun.* **10**, 1–7 (2019).
37. Yablonovitch, E. Photonic crystals. *J. Mod. Opt.* **41**, 173–194 (1994).
38. Sakoda, K. Optical properties of photonic crystals. *Springer Science & Business Media* **80** (2004).
39. Yang, M., Chen, S., Fu, C. & Sheng, P. Optimal sound-absorbing structures. *Mater. Horiz.* **4**, 673–680 (2017).
40. Yang, M. et al. Subwavelength total acoustic absorption with degenerate resonators. *Appl. Phys. Lett.* **107**, 104104 (2015).
41. Oh, J. H., Qi, S., Kim, Y. Y. & Assouar, B. Elastic metamaterial insulator for broadband low-frequency flexural vibration shielding. *Phys. Rev. Appl.* **8**, 054034 (2017).
42. Lee, S. W. & Oh, J. H. Abnormal Stop Band Behavior Induced by Rotational Resonance in Flexural Metamaterial. *Sci. Rep.* **8**, 1–13 (2018).
43. Chen, H. & Chan, C. Acoustic cloaking in three dimensions using acoustic metamaterials. *Appl. Phys. Lett.* **91**, 183518 (2007).
44. Torrent, D. & Sánchez-Dehesa, J. Acoustic cloaking in two dimensions: a feasible approach. *N. J. Phys.* **10**, 063015 (2008).
45. Williams, E. G., Roux, P., Rupin, M. & Kuperman, W. Theory of multiresonant metamaterials for A 0 lamb waves. *Phys. Rev. B* **91**, 104307 (2015).
46. Lee, D., Oh, J. H., Kang, I. S. & Rho, J. Seismic phononic crystals by elastodynamic Navier equation. *Phys. Rev. E* **100**, 063002 (2019).
47. Cha, J. & Daraio, C. Electrical tuning of elastic wave propagation in nanomechanical lattices at MHz frequencies. *Nat. Nanotechnol.* **13**, 1016–1020 (2018).
48. Garcia, C. R. et al. 3D printing of anisotropic metamaterials. *Prog. Electromagnetics Res. Lett.* **34**, 75–82 (2012).
49. Lei, M. et al. 3D printing of auxetic metamaterials with digitally reprogrammable shape. *ACS Appl. Mater. Interfaces* **11**, 22768–22776 (2019).
50. Chen, Z., Guo, B., Yang, Y. & Cheng, C. Metamaterials-based enhanced energy harvesting: A review. *Phys. B: Condens. Matter* **438**, 1–8 (2014).
51. Hu, G., Tang, L., Liang, J., Lan, C. & Das, R. Acoustic-Elastic Metamaterials and Phononic Crystals for Energy Harvesting: A Review. *Smart Mater. Struct.* **30**, 085025 (2021).
52. Liu, Z. et al. Locally resonant sonic materials. *Science* **289**, 1734–1736 (2000).
53. Huang, H., Sun, C. & Huang, G. On the negative effective mass density in acoustic metamaterials. *Int. J. Eng. Sci.* **47**, 610–617 (2009).
54. Meade, R. D., Rappé, A., Brommer, K., Joannopoulos, J. & Alerhand, O. Accurate theoretical analysis of photonic band-gap materials. *Phys. Rev. B* **48**, 8434 (1993).
55. Achaoui, Y., Khelif, A., Benchabane, S., Robert, L. & Laude, V. Experimental observation of locally-resonant and Bragg band gaps for surface guided waves in a phononic crystal of pillars. *Phys. Rev. B* **83**, 104201 (2011).
56. Xiao, Y., Wen, J., Wang, G. & Wen, X. Theoretical and experimental study of locally resonant and Bragg band gaps in flexural beams carrying periodic arrays of beam-like resonators. *Journal of Vibration and Acoustics* **135** (2013).
57. Yuan, B., Humphrey, V. F., Wen, J. & Wen, X. On the coupling of resonance and Bragg scattering effects in three-dimensional locally resonant sonic materials. *Ultrasonics* **53**, 1332–1343 (2013).
58. Gonella, S., To, A. C. & Liu, W. K. Interplay between phononic bandgaps and piezoelectric microstructures for energy harvesting. *J. Mech. Phys. Solids* **57**, 621–633 (2009).
59. Mikoshiba, K., Manimala, J. M. & Sun, C. Energy harvesting using an array of multifunctional resonators. *J. Intell. Mater. Syst. Struct.* **24**, 168–179 (2013).
60. Ahmed, R. U. & Banerjee, S. Low frequency energy scavenging using sub-wave length scale acousto-elastic metamaterial. *AIP Adv.* **4**, 117114 (2014).
61. Li, Y., Baker, E., Reissman, T., Sun, C. & Liu, W. K. Design of mechanical metamaterials for simultaneous vibration isolation and energy harvesting. *Appl. Phys. Lett.* **111**, 251903 (2017).
62. Li, J., Zhou, X., Huang, G. & Hu, G. Acoustic metamaterials capable of both sound insulation and energy harvesting. *Smart Mater. Struct.* **25**, 045013 (2016).
63. Chen, J.-S., Su, W.-J., Cheng, Y., Li, W.-C. & Lin, C.-Y. A metamaterial structure capable of wave attenuation and concurrent energy harvesting. *J. Intell. Mater. Syst. Struct.* **30**, 2973–2981 (2019).
64. De Espinosa, F. M., Jimenez, E. & Torres, M. Ultrasonic band gap in a periodic two-dimensional composite. *Phys. Rev. Lett.* **80**, 1208 (1998).
65. Hou, Z., Fu, X. & Liu, Y. Singularity of the Bloch theorem in the fluid/solid phononic crystal. *Phys. Rev. B* **73**, 024304 (2006).
66. Painter, O. et al. Two-dimensional photonic band-gap defect mode laser. *Science* **284**, 1819–1821 (1999).
67. Khelif, A., Wilm, M., Laude, V., Ballandras, S. & Djafari-Rouhani, B. Guided elastic waves along a rod defect of a two-dimensional phononic crystal. *Phys. Rev. E* **69**, 067601 (2004).
68. Langer, J. M. & Heinrich, H. Deep-level impurities: A possible guide to prediction of band-edge discontinuities in semiconductor heterojunctions. *Phys. Rev. Lett.* **55**, 1414 (1985).
69. Pond, R. & Hirth, J. Defects at surfaces and interfaces. *Solid State Phys.* **47**, 287–365 (1994).
70. Wen, X.-G. Topological orders in rigid states. *Int. J. Mod. Phys. B* **4**, 239–271 (1990).
71. Wu, L.-Y., Chen, L.-W. & Liu, C.-M. Acoustic energy harvesting using resonant cavity of a sonic crystal. *Appl. Phys. Lett.* **95**, 013506 (2009).
72. Wang, W.-C., Wu, L.-Y., Chen, L.-W. & Liu, C.-M. Acoustic energy harvesting by piezoelectric curved beams in the cavity of a sonic crystal. *Smart Mater. Struct.* **19**, 045016 (2010).
73. Lv, H., Tian, X., Wang, M. Y. & Li, D. Vibration energy harvesting using a phononic crystal with point defect states. *Appl. Phys. Lett.* **102**, 034103 (2013).
74. Chuang, K.-C., Zhang, Z.-Q. & Wang, H.-X. Experimental study on slow flexural waves around the defect modes in a phononic crystal beam using fiber Bragg gratings. *Phys. Lett. A* **380**, 3963–3969 (2016).
75. Oudich, M. & Li, Y. Tunable sub-wavelength acoustic energy harvesting with a metamaterial plate. *J. Phys. D: Appl. Phys.* **50**, 315104 (2017).

76. Lee, D. et al. Underwater stealth metasurfaces composed of split-orifice-conduit hybrid resonators. *J. Appl. Phys.* **129**, 105103 (2021).
77. Ma, K. et al. Metamaterial and Helmholtz coupled resonator for high-density acoustic energy harvesting. *Nano Energy* **82**, 105693 (2021).
78. Park, C.-S. et al. Two-dimensional octagonal phononic crystals for highly dense piezoelectric energy harvesting. *Nano Energy* **57**, 327–337 (2019).
79. Iga, K. Theory for gradient-index imaging. *Appl. Opt.* **19**, 1039–1043 (1980).
80. Moore, D. T. Gradient-index optics: a review. *Appl. Opt.* **19**, 1035–1038 (1980).
81. Hassani, B. & Hinton, E. A review of homogenization and topology optimization I—homogenization theory for media with periodic structure. *Computers Struct.* **69**, 707–717 (1998).
82. Kung, S.-Y., Arun, K. S. & Rao, D. B. State-space and singular-value decomposition-based approximation methods for the harmonic retrieval problem. *J. Optical Soc. Am.* **73**, 1799–1811 (1983).
83. Lin, S.-C. S., Huang, T. J., Sun, J.-H. & Wu, T.-T. Gradient-index phononic crystals. *Phys. Rev. B* **79**, 094302 (2009).
84. Darabi, A. & Leamy, M. J. Analysis and experimental validation of an optimized gradient-index phononic-crystal lens. *Phys. Rev. Appl.* **10**, 024045 (2018).
85. Tol, S., Degertekin, F. L. & Erturk, A. Gradient-index phononic crystal lens-based enhancement of elastic wave energy harvesting. *Appl. Phys. Lett.* **109**, 063902 (2016).
86. Lin, Z. & Tol, S. Elastic metasurfaces for full wavefront control and low-frequency energy harvesting. *J. Vib. Acoust.* **143**, 061005 (2021).
87. Tol, S., Degertekin, F. L. & Erturk, A. Low-frequency elastic wave focusing and harvesting via locally resonant metamaterials. *Smart Materials, Adaptive Structures and Intelligent Systems* (2017).
88. Tol, S., Degertekin, F. & Erturk, A. Phononic crystal Luneburg lens for omnidirectional elastic wave focusing and energy harvesting. *Appl. Phys. Lett.* **111**, 013503 (2017).
89. Zareei, A., Darabi, A., Leamy, M. J. & Alam, M.-R. Continuous profile flexural GRIN lens: Focusing and harvesting flexural waves. *Appl. Phys. Lett.* **112**, 023901 (2018).
90. Hyun, J., Choi, W. & Kim, M. Gradient-index phononic crystals for highly dense flexural energy harvesting. *Appl. Phys. Lett.* **115**, 173901 (2019).
91. Tol, S., Degertekin, F. & Erturk, A. 3D-printed phononic crystal lens for elastic wave focusing and energy harvesting. *Addit. Manuf.* **29**, 100780 (2019).
92. Allam, A., Sabra, K. & Erturk, A. Sound energy harvesting by leveraging a 3D-printed phononic crystal lens. *Appl. Phys. Lett.* **118**, 103504 (2021).
93. Jo, S.-H., Yoon, H., Shin, Y. C. & Youn, B. D. An analytical model of a phononic crystal with a piezoelectric defect for energy harvesting using an electroelastically coupled transfer matrix. *Int. J. Mech. Sci.* **193**, 106160 (2021).
94. Jo, S.-H., Yoon, H., Shin, Y. C. & Youn, B. D. Revealing defect-mode-enabled energy localization mechanisms of a one-dimensional phononic crystal. *Int. J. Mech. Sci.* **215**, 106950 (2021).
95. Wang, Z. & Li, T. A semi-analytical model for energy harvesting of flexural wave propagation on thin plates by piezoelectric composite beam resonators. *Mech. Syst. Signal Process.* **147**, 107137 (2021).
96. Jo, S.-H. & Youn, B. D. A Phononic Crystal with Differently Configured Double Defects for Broadband Elastic Wave Energy Localization and Harvesting. *Crystals* **11**, 643 (2021).
97. Xie, Y., Konneker, A., Popa, B.-I. & Cummer, S. A. Tapered labyrinthine acoustic metamaterials for broadband impedance matching. *Appl. Phys. Lett.* **103**, 201906 (2013).
98. Lan, C., Hu, G., Tang, L. & Yang, Y. Energy localization and topological protection of a locally resonant topological metamaterial for robust vibration energy harvesting. *J. Appl. Phys.* **129**, 184502 (2021).
99. Wen, Z. et al. Topological cavities in phononic plates for robust energy harvesting. *Mech. Syst. Signal Process.* **162**, 108047 (2022).
100. Chong, C. et al. Nonlinear vibrational-state excitation and piezoelectric energy conversion in harmonically driven granular chains. *Phys. Rev. E* **93**, 052203 (2016).
101. Lu, Z.-Q., Zhao, L., Ding, H. & Chen, L.-Q. A dual-functional metamaterial for integrated vibration isolation and energy harvesting. *J. Sound Vib.* 116251 (2021).

Acknowledgements

This work was financially supported by the POSCO-POSTECH-RIST Convergence Research Center program funded by POSCO, the National Research Foundation of Korea (NRF) grants (NRF-2019R1A2C3003129, CAMM2019M3A6B3030637, NRF-2019R1A5A8080290) funded by the Ministry of Science and ICT of the Korean government, and the grant (PES4400) from the endowment project of “Development of smart sensor technology for underwater environment monitoring” funded by Korea Research Institute of Ships & Ocean engineering (KRISO). G.L. acknowledges the Hyundai Motor *Chung Mong-Koo* fellowship. D.L. acknowledges the NRF Global Ph.D. fellowship (NRF-2018H1A2A1062053) funded by the Ministry of Education of the Korean government.

Author contributions

J.R. conceived the idea and initiated the project. G.L., D.L., Y.J., M.K., and J.R. wrote the manuscript. G.L. and J.P. prepared the figures. All authors read and provided feedback on the manuscript. J.R. guided the entire work.

Competing interests

The authors declare no competing interests.

Additional information

Correspondence and requests for materials should be addressed to Junsuk Rho.

Peer review information *Communications Physics* thanks Serife Tol and the other, anonymous, reviewer(s) for their contribution to the peer review of this work.

Reprints and permission information is available at <http://www.nature.com/reprints>

Publisher's note Springer Nature remains neutral with regard to jurisdictional claims in published maps and institutional affiliations.



Open Access This article is licensed under a Creative Commons Attribution 4.0 International License, which permits use, sharing, adaptation, distribution and reproduction in any medium or format, as long as you give appropriate credit to the original author(s) and the source, provide a link to the Creative Commons license, and indicate if changes were made. The images or other third party material in this article are included in the article's Creative Commons license, unless indicated otherwise in a credit line to the material. If material is not included in the article's Creative Commons license and your intended use is not permitted by statutory regulation or exceeds the permitted use, you will need to obtain permission directly from the copyright holder. To view a copy of this license, visit <http://creativecommons.org/licenses/by/4.0/>.

© The Author(s) 2022